



TECHNISCHE  
UNIVERSITÄT  
WIEN



## DIPLOMARBEIT

# Determination of the neutron flux distribution for the CRAB experiment at Atominstitut

im Rahmen des Studiums  
**Technische Physik**

eingereicht von

**Florian Engel**

Matrikelnummer: 01608674

ausgeführt am

Atominstitut der Fakultät für Physik der Technischen Universität Wien

Betreuung:

Privatdoz. Dipl.-Ing. Dr.techn. Stephan Sponar (TU Wien / Atominstitut)

Ass.Prof. Dipl.-Ing. Dr.techn. Jericha Erwin (TU Wien / Atominstitut)

Wien, August 28, 2024

---

(Unterschrift Verfasserin)

---

(Unterschrift Betreuer)

## Abstract

The scope of this master thesis is to accurately determine the detector efficiencies of multiple gas proportional counters which are in use at Atominstitut. To achieve this goal, multiple experiments have been performed: The spectral distribution of the neutron beam used was determined by neutron time-of-flight spectroscopy. A neutron activation analysis of Indium samples provided data about the absolute neutron flux present. The efficiencies of the characterised detectors was then experimentally determined by comparing their measured fluxes to the absolute flux present. Furthermore an analytical formula for calculating the efficiency of a gas-filled neutron detector with or without apertures was tested with those measurements. Additionally, an alternative to the currently used software for the readout of gamma detectors was tested as well.

The results showed good agreement between the analytical formula for detector efficiency and the experimental results; the predicted efficiencies mostly are within  $\pm\sigma$  of the experimental values. A table for common aperture sizes and the corresponding expected efficiencies has been compiled to allow for quick use and save time on those calculations in the future. It was observed that the assumption of a monochromatic thermal neutron beam may be justified for application with lower required precision. Despite consisting of multiple wavelengths, the detector response was quite close to the expectation for a thermal neutron beam.

## Zusammenfassung

Das Ziel dieser Masterarbeit ist es, die Detektoreffizienz mehrerer Gasproportionalzähler die am Atominstitut verwendet werden, so genau wie möglich zu bestimmen. Um dieses Ziel zu erreichen wurden mehrere Experimente durchgeführt. Die spektrale Verteilung des Neutronenstrahles wurde mittels Flugzeitspektroskopie bestimmt. Eine Neutronenaktivierungsanalyse wurde an mehreren Indiumsonden durchgeführt, um einen Referenzwert für den absoluten vorhandenen Neutronenfluss zu erhalten. Die Effizienzen der untersuchten Detektoren wurden experimentell bestimmt, indem der von ihnen gemessene Fluss mit dem absoluten vorhandenen Fluss verglichen wurde. Weiters wurde eine analytische Formel zur Berechnung der Detektoreffizienz für gasgefüllte Neutronendetektoren mit und ohne Blenden getestet. Außerdem wurde eine alternative für die momentan verwendete Software zum Auslesen der Resultate von Gammadetektoren getestet.

Die Resultate zeigen gute Übereinstimmungen zwischen den theoretischen Erwartungen der Formel für Detektoreffizienz und den experimentellen Ergebnissen; die vorhergesagten Effizienzen befinden sich größtenteils innerhalb von  $\pm\sigma$  um die experimentellen Werte. Eine Tabelle für übliche Blendengrößen und deren zugehörigen Detektoreffizienzen wurde erstellt um in Zukunft Zeit für Berechnungen sparen zu können. Es wurde ferner beobachtet, dass der untersuchte Neutronenstrahl scheinbar für Anwendungen mit geringerer benötigter Genauigkeit durchaus als vollständig monochromatisch und thermisch angenommen werden kann. Während dies streng genommen nicht der Fall ist, da er sich eigentlich aus mehreren Wellenlängen zusammensetzt, sind die experimentellen Effizienzen nahe an den Vorhersagen der Formel für thermische Neutronen.

# Contents

<b>Abstract</b>	<b>2</b>
<b>Zusammenfassung</b>	<b>3</b>
<b>1 Introduction</b>	<b>5</b>
<b>2 Physical background</b>	<b>7</b>
2.1 Measuring the spectral distribution of the neutron flux . . . . .	7
2.2 Neutron activation analysis . . . . .	8
2.3 Neutron detection with gas filled proportional counters . . . . .	11
2.4 Detector efficiency . . . . .	12
<b>3 Material an Methods</b>	<b>17</b>
3.1 Measurement setup . . . . .	17
3.1.1 Neutron time-of-flight measurements . . . . .	17
3.1.2 Neutron activation analysis . . . . .	18
3.1.3 Measuring with different gas proportional counters . . . . .	20
3.2 Utilized neutron detectors . . . . .	23
3.2.1 VacuTec Type 70 063 . . . . .	23
3.2.2 Canberra 20NH20/1TP . . . . .	25
3.2.3 Canberra 0.5NH1/1KF . . . . .	27
3.2.4 Reuter Stokes BF <sub>3</sub> -counter . . . . .	29
3.3 Spectral radiation analysis software "InterSpec" v1.0.11 . . . . .	30
<b>4 Results</b>	<b>35</b>
4.1 Neutron activation analysis . . . . .	35
4.2 Spectral distribution of the neutron beam . . . . .	36
4.3 Detector efficiency of various gas filled proportional counters . . . . .	48
4.4 Evaluation of the neutron radiography image . . . . .	49
<b>5 Discussion</b>	<b>51</b>
5.1 Neutron activation analysis . . . . .	51
5.2 Spectral analysis of the neutron beam . . . . .	52
5.3 Detector efficiency of various gas filled proportional counters . . . . .	54
<b>6 Conclusion</b>	<b>57</b>
<b>List of Figures</b>	<b>59</b>
<b>List of Tables</b>	<b>61</b>
<b>References</b>	<b>62</b>

# 1 Introduction

While neutron detection is done regularly at Atominstitut, some characteristics of the used detectors are not entirely known. Even though usually some parameters for sensitivity of the detectors are given by the fabricator, those mostly refer to some very specific setting. When used in different settings, the detector efficiency may vary by quite a large margin. While this is not an issue when one is interested in qualitative results, it makes it difficult to actually quantise measurements.

For the CRAB project (Calibration by Recoils for Accurate Bolometry) [1][2] currently running, quantitative knowledge of the neutron beam is of importance. The scope of the CRAB project is the calibration of a cryogenic detector for either coherent elastic neutrino-nucleus scattering or the detection of light dark matter candidates. Those are used at the NUCLEUS experiment at the Chooz nuclear power plant in France for measuring reactor anti-neutrinos  $\bar{\nu}_e$  [3][4]. The detectors in question are small  $\text{CaWO}_4$  crystals operated as transition edge sensors. Transition edge sensors generally are operated at the border region of the superconducting phase, where the heat capacity is small enough that even the smallest amounts of deposited energy leads to detectable temperature changes [5]. This  $\Delta T$  is measured indirectly through the change of resistivity of the detector. The changing resistivity induces a change in a connected inductance and the corresponding change in magnetic flux is then detected with a SQUID. In that way, the energy of nuclear recoils can be measured with high energy resolution. Future applications for NUCLEUS type detectors in reactor instrumentation and monitoring or in probing the standard model physics and searching for dark matter make this specific detector type object of current research.

The nuclear recoils in question are of very low energies, the detector needs to be able to resolve structures at 100 eV and below. Accurate calibration methods are needed and shall be provided by the CRAB project. CRAB proposes the use of thermal neutron capture as induced calibration signal. This would potentially allow for on-site calibration of NUCLEUS detectors. Thermal neutrons have kinetic energies around 25 meV, which can be neglected compared to the nuclear recoils. The actual nuclear recoil is created when a Tungsten captured a neutron and then de-excites by emission of a high energy  $\gamma$ . Due to the high energy of the emitted photons, it is very likely that they escape the small detector volume (5 mm  $\times$  5 mm  $\times$  5 mm) so the only energy remaining in the detector is the energy of the nuclear recoil from the gamma emission. If one measures not only the deposited energy but also the escaping photon it is possible to correlate those events, leading to an improved resolution. While de-excitation via single  $\gamma$ -emission is not the only channel, the induced signals via gamma cascades can be used as additional calibration lines.

The maximum count rate the detector can withstand is narrowly constrained by the decay time of the detector pulses. Following measurements of the CRAB collaboration, the desired neutron flux on the detector was determined to be  $270 \text{ cm}^{-2}\text{s}^{-1}$ . As a result,

it is necessary to manipulate the tangential neutron beam at Atominstitut, which will be used for CRAB, to produce this desired flux. To ensure that the expected flux is actually achieved, it is necessary to have the ability for measuring the present neutron flux on site on demand.

Determining both present neutron flux and spectral distribution therefore is of great interest for the future. While some measurements about the spatial distribution of the main neutron beam were already performed using  $^3\text{He}$ -counters [6][7] and first calculations were made, the developed analytical formula needs thorough examination and experimental validation. Furthermore, the actual CRAB beamline is still being set up and new flux measurements need to be taken when the experiment starts. As a byproduct, this was a good opportunity to revisit measurements commonly performed during the Neutronenpraktikum and further improve on their results.

To achieve a good understanding of detector responses of the neutron detectors commonly used at Atominstitut, a combination of various methods and a analytical formula for calculating detector efficiencies are applied. First and foremost, the present neutron spectrum is determined by neutron time-of-flight measurements, characterizing the wavelengths present in the beam. Using the analytical formula allows to obtain not only the wavelengths but also an estimate of their contribution to the neutron beam. This leads to precise knowledge of the beam we are working with. A neutron activation analysis is then performed to determine the absolute present neutron flux. This method is well known and often practised at the institute, usually under the assumption of a monochromatic neutron beam. An adapted version is used to accommodate for multiple wavelengths. The obtained flux then can be compared to the flux measured by each detector, giving empirical values for the detector efficiencies in the used setting. Comparison with the results of the analytical formula on the other hand puts a perspective on the accuracy of the formula. Especially the influence of apertures in combination with cylindrical detectors is examined in this thesis. As the Atominstitut provides the unique opportunity to perform neutron radiography, it was also attempted to apply this method for estimating the efficiency of one of the used detectors in a white neutron beam.

## 2 Physical background

### 2.1 Measuring the spectral distribution of the neutron flux

An established technique to determine the spectral distribution of neutrons are time of flight measurements (n-TOF). This type of measurement determines present neutron energies by measuring the time they need for passing a known distance.

The used beamline is located at the tangential beam tube of the research reactor and provides thermal neutrons. A graphite monochromator crystal selects certain wavelengths of the white neutron spectrum according to the Bragg Law,

$$n\lambda = 2d \sin(\theta), \quad n \in \mathbb{N} \quad (2.1)$$

and an approximation of a monochromatic neutron beam is achieved. However, as can easily be seen from this equation, the beam is not necessarily strictly monochromatic, as integer factors of the passing wavelength  $\lambda$  are allowed.

Neutron wavelength is correlated to momentum and therefore speed. Hence we need to measure the time  $\Delta t$  our neutrons need for various known distances  $\Delta s$ . This is easily achieved using a pulsed neutron beam. To create a pulsed neutron beam from the continuous beam provided by the reactor, a chopper was used. It consists of a rotating cylinder made from layers of a strong neutron absorber with a material transparent to neutrons in the middle. The cylinder rotates at a known frequency of 50 Hz. The distances  $\Delta s$  are determined by the positioning of detector and chopper. The time needed for the distance is measured as a  $\Delta t$  between the chopper rotating into an open position, detected by a light barrier, and the actual neutron detection by a  $^3\text{He}$ -counter. Measurements for different distances between chopper and neutron counter yield different  $\Delta t$ , giving information about the neutrons speed (and therefore energy and wavelength). For a monochromatic neutron beam, we expect a single peak at a specific  $\Delta t$ , as all neutrons are supposed to have the same energy. If multiple different wavelengths are present as eq. (2.1) suggests, multiple peaks at different values of  $\Delta t$  will be found. When plotting counted neutrons as a function of  $\Delta t$ , each peak represents a neutron energy. The position of the maximum is the time a neutron needs to reach the detector after passing the chopper. With known distances, calculating the neutrons momenta and wavelengths is a straightforward task. In order to determine which fraction of the beam each neutron energy makes, one can compare the areas under each peak. Here it should be considered, that the detection efficiency depends on the neutron energy via the absorption cross section. With known distance and time, the neutrons speed and furthermore their wavelength can be calculated as

$$\lambda = \frac{h \cdot \Delta t}{m_n \cdot \Delta s} = \frac{h}{m_n \cdot v_n} = \frac{h}{p} \quad (2.2)$$

Naturally, the peaks recorded have a certain width. This comes from two effects: Firstly, the opening window of the chopper has a finite size. This gives the peak a certain natural width. The other parameter determining the peak width is the dispersion of the neutrons, additionally broadening the peak. If multiple wavelengths are present in the

neutron beam, we detect multiple peaks. Those may be combined into one single, bigger peak for short distances between detector and chopper due to the aforementioned finite line width. With increasing distance between the components, more peaks can be resolved. In addition to the different wavelengths present in the beam, it is furthermore possible to determine the beam composition by comparing the amounts of neutrons with the different speeds.

## 2.2 Neutron activation analysis

The core task of this thesis is to determine the neutron flux of the CRAB beam as precisely as possible. In order to reach that goal it has been necessary to determine the detector efficiencies of various  $^3\text{He}$  proportional counters and a  $\text{BF}_3$  proportional counter as precise as possible. In order to physically measure the different efficiencies, it is necessary to get a good estimate of the actually present neutrons in the first place. This was achieved by performing a neutron activation analysis on an Indium sample. When exposed to thermal neutrons, Indium atoms can capture a neutron and go through a radioactive decay process. When this decay occurs, characteristic gamma radiation is emitted. Those photons can then be captured by an already well characterised detector. With the taken gamma spectrum it is possible to calculate the amount of neutrons necessary to produce the measured excitation. The neutron flux is directly proportional to the intensity of a characteristic gamma line. The proportionality constant can be said to consist of mostly probability factors, which shall be explained below:

Firstly, the efficiency of the detector used to gather the gamma spectrum has to be considered. It depends on multiple factors like geometry and impacting  $\gamma$  energy.

$$n_{\gamma,\text{emitted}}(E_\gamma) = \frac{n_{\gamma,\text{detected}}(E_\gamma)}{\eta_{\text{Detector}}(E_\gamma)} \quad (2.3)$$

Here  $n_{\gamma,\text{emitted}}(E_\gamma)$  is the number of gammas that were actually emitted at a chosen energy  $E_\gamma$ ,  $n_{\gamma,\text{detected}}$  is the amount of photons the detector actually registered and  $\eta_{\text{Detector}}(E_\gamma)$  describes the detector efficiency, which consists of the actual energy-dependent efficiency, the fraction of the total solid angle covered and the ratio of detector live time divided by real time to correct for the detectors dead time. In a fixed sample-detector arrangement the first 2 factors may be combined into a single energy-dependent effective efficiency. The second factor to consider is the probability, that a characteristic gamma is emitted. This varies depending on the used element.  $^{115}\text{In}$  was chosen as probe material due to the decay scheme of the activated  $^{116}\text{In}$ , which can be seen in Figure 2.1. Additionally, an interactive chart of this decay with the ability to highlight single gammas or energy levels can be found at [8]. As visible in Figure 2.1, the decay modes we focus on is not the only possibility for an excited Indium nucleus to get rid of its excess energy. Three excited states with different half-lives can be observed. However, those states do not live for long enough to produce measurable gamma intensities in this experiment, because

during transit of the sample from the reactor hall to the gamma detector more than 10 half-lives pass and basically zero activity is left from those states. The 8<sup>-</sup>-state actually decays into the 5<sup>+</sup>-state, which is the one relevant for evaluation.

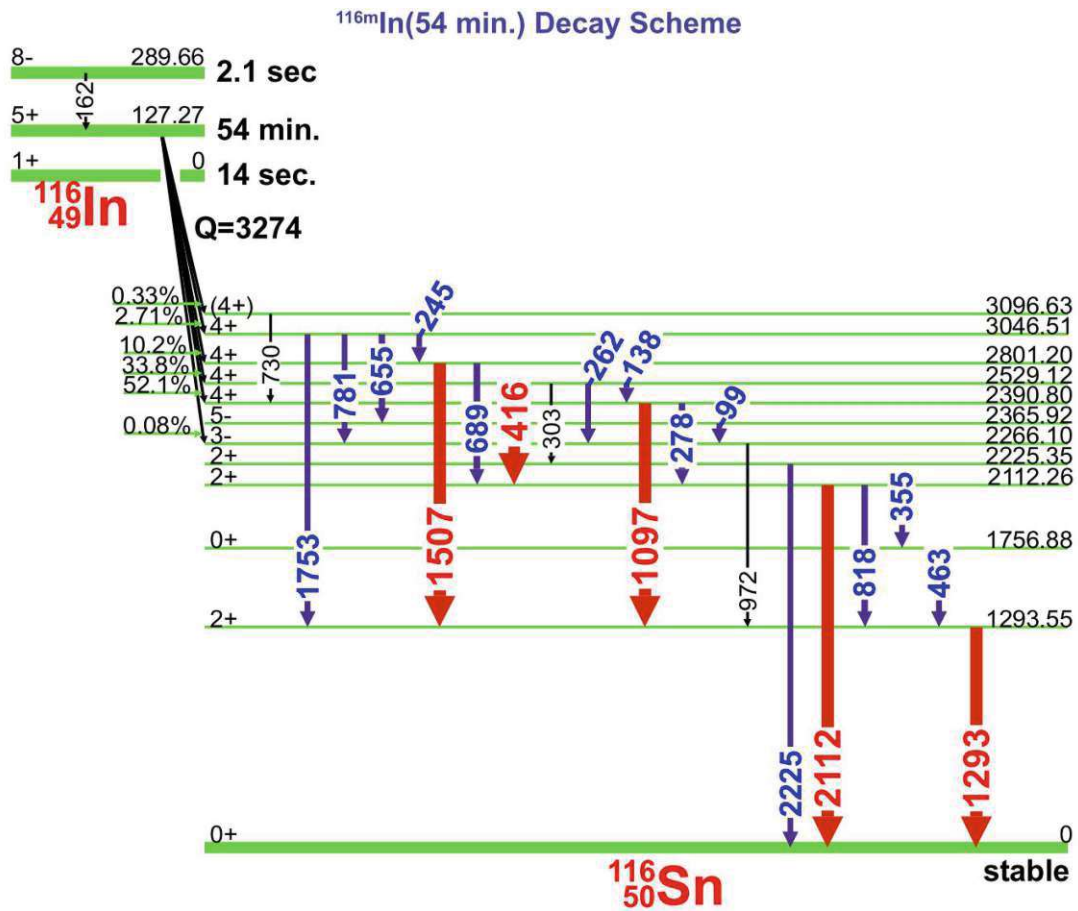


**Figure 2.1:** Decay scheme of <sup>116</sup>In [9]. The red arrows signify the characteristic gamma energies used to calculate the neutron flux. The blue and black arrows show minor nuclear transitions; their probabilities to occur are too small to give statistically relevant results. Transition energies are given in keV.

As can be observed in Figure 2.1, <sup>116</sup>In has five major characteristic gamma lines. Their energies and the corresponding probabilities that they occur at a decay are tabulated below.

The existence of multiple characteristic gamma lines gives the possibility to have a consistency check built in to the for the performed measurements and evaluation, as the calculated neutron flux should be the same for each of those gamma lines. A disadvantage of this choice of material however is that the total amount of counted photons is

Gamma Energy $E_\gamma$ [keV]	Line probability $I_\gamma(E_\gamma)$ [%]
416	27.7
1097	56.2
1293	84.4
1507	10.0
2112	15.5

**Table 2.1:** Energies of characteristic gammas and probabilities that they occur in a decay of  $^{116}\text{In}$  [9].

distributed among five different energies, while for example  $^{198}\text{Au}$  has only one characteristic gamma line where all photons produced by nuclear decay would pile up. Due to the large discrepancy in half life of those two elements, Indium was ultimately selected as the more practical candidate.

To continue the evaluation,

$$n_{\text{reactions}} = \frac{n_{\gamma,\text{emitted}}(E_\gamma)}{I_\gamma(E_\gamma)} \quad (2.4)$$

equation (2.4) calculates the number of nuclear decay processes that occurred during the gamma measurement, taking the number of gamma photos that were actually emitted from equation (2.3) and properly scaling it with the line probability  $I_\gamma$  from Table 2.1.

We can now simply obtain the activity of our probe

$$A = n_{\text{reactions}} \cdot \frac{\lambda}{1 - e^{-\lambda t_{\text{measurement}}}} \quad (2.5)$$

with  $\lambda$  being the known decay constant of  $^{116}\text{In}$  and  $t_{\text{measurement}}$  being the duration of the gamma measurement. To finally obtain the neutron flux, the result from equation (2.5) needs to be corrected by the amount of nuclei which decayed during transit from the reactor hall to the gamma detector (decay time  $t_{\text{decay}}$ ), the survival probability of an  $^{116}\text{In}$  during the irradiation (irradiation time  $t_{\text{irr}}$ ) and the self-shielding factor  $G$  of the probe[10]. This activity is proportional to the neutron flux  $\phi$ , the thermal capture cross section  $\sigma_a$  and the number of atoms exposed to the neutron beam  $n_{\text{In}}$ . We therefore divide it by the thermal capture cross section and the number of atoms exposed to radiation. The result now is the neutron flux responsible for the activation of the Indium probe:

$$\phi = \frac{A \cdot e^{\lambda t_{\text{decay}}}}{G n_{\text{In}} \sigma_a (1 - e^{-\lambda t_{\text{irr}}})} \quad (2.6)$$

It is noteworthy that this formula assumes a monochromatic neutron beam of thermal neutrons, as the thermal absorption cross section  $\sigma_a$  is used. This circumstance can be corrected by using a superposition of the actual cross-sections, weighted by their relative occurrence, determined in subsection 4.2.

### 2.3 Neutron detection with gas filled proportional counters

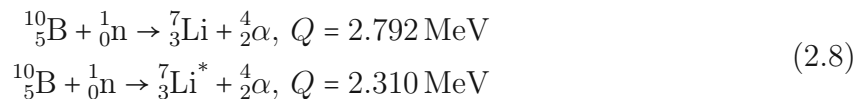
For the detection of thermal neutrons, materials with high neutron absorption cross sections at low incident energies are used. Examples can be seen in Figure 2.2.

In a  $^3\text{He}$  proportional counter, neutrons are detected indirectly via the  $^3\text{He}(n,p)$ -reaction (corresponding absorption cross-section for thermal neutrons (2200 m/s):  $\sigma_a = 5333 \text{ b}$ )[11][12]:



An alternative to the rare  $^3\text{He}$  gas can be found in  $^{10}\text{B}$  which has a natural abundance of 19.65% and a corresponding absorption cross-section for thermal neutrons (2200 m/s) of  $\sigma_a = 3837 \text{ b}$ [12][13] It has been traditionally used in the form of the gas  $\text{BF}_3$ . fluorine has a negligible neutron capture cross section and therefore does not contribute to the detector signal. In modern detectors, this corrosive gas is less popular and the boron is used in solid state [14][15][16].

For  $^{10}\text{B}$ , two neutron capture reactions are possible:



The first reaction produces a  $^7_3\text{Li}$  in its ground state while the second reaction produces an

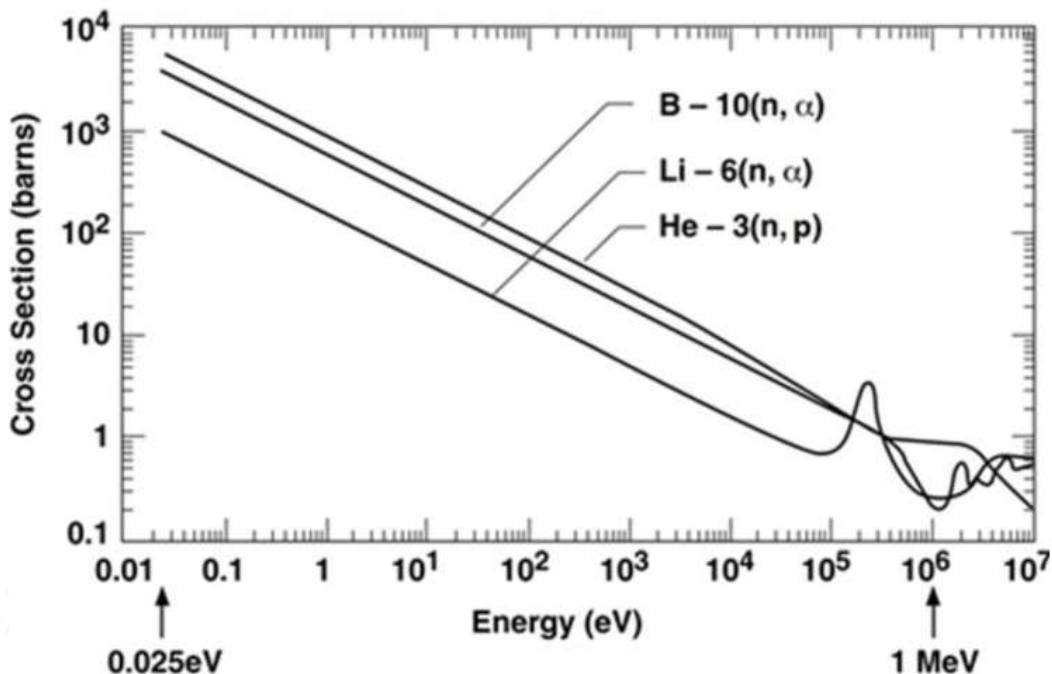


Figure 2.2: Neutron absorption cross-section  $\sigma_a$  for  $^3\text{He}$ ,  $^{10}\text{B}$  and  $^6\text{Li}$  as a function of incident neutron Energy [17].

excited  ${}^7_3\text{Li}$ . The excited lithium core then falls back to its ground state, emitting a gamma which escapes the active detector volume without causing other excitations, hence it can be neglected. The energetic particles stemming from either  ${}^3\text{He}$  or  ${}^{10}\text{B}$  neutron capture reactions cause ionisation within the filling gas. Those charges can now be collected and counted by applying a high voltage. The resulting signal is a pulse of measurable voltage which is directly proportional to the amount of energy deposited by the nuclear reaction. Each pulse represents one neutron.

Due to conservation of momentum, both the products of the nuclear reaction move in opposite directions. In comparison with the Q values, the kinetic energy of the neutrons and therefore also their momenta may be neglected. As a real detector has finite dimensions, one of the reaction products may be absorbed by the detector wall before it can deposit all of its kinetic energy. This so called "wall effect" has an effect on the recorded voltage spectra: besides the full energy peak (where all the kinetic energy of the reaction products - proton and triton or lithium and  $\alpha$  respectively - is deposited within the detector medium), there are two plateaus. Those represent events where at least one of both products deposits its full energy within the detector volume: the first plateau is the result of the heavier reaction product depositing its full energy and the lighter reaction product deposits only a fraction of its energy. The second plateau is the result of the lighter reaction product depositing its full energy and the heavier reaction product only depositing a fraction of its energy. Figure 2.3 shows an example spectrum of the used VacuTec  ${}^3\text{He}$ -counter with full energy peak and wall effects.

## 2.4 Detector efficiency

A theoretical formula to determine detector efficiency of cylindrical gas-filled proportional counters with a rectangular aperture was already derived in [7]:

We start at the formula for neutrons passing through matter [11],

$$N(x) = N_0 \cdot e^{-x/\lambda_a}$$

$$\text{with } \lambda_a = \frac{M}{N_A \rho \sigma_a} \quad (2.9)$$

$N(x)$  is the number of neutrons of a beam with initial neutron count  $N_0$  after passing through a material with thickness  $x$ .  $M$  is the molar mass of the absorbing medium, which will be  ${}^3\text{He}$  or  ${}^{10}\text{B}$ .  $N_A$  is the Avogadro constant,  $\rho$  the mass density of the detector medium, and  $\sigma_a$  the cross section for absorption of a neutron in the medium. For further simplification, the Avogadro constant can be taken out of the equation, as it is contained within the molar mass, resulting in:

$$\lambda_a = \frac{m}{\rho \sigma_a} \quad (2.10)$$

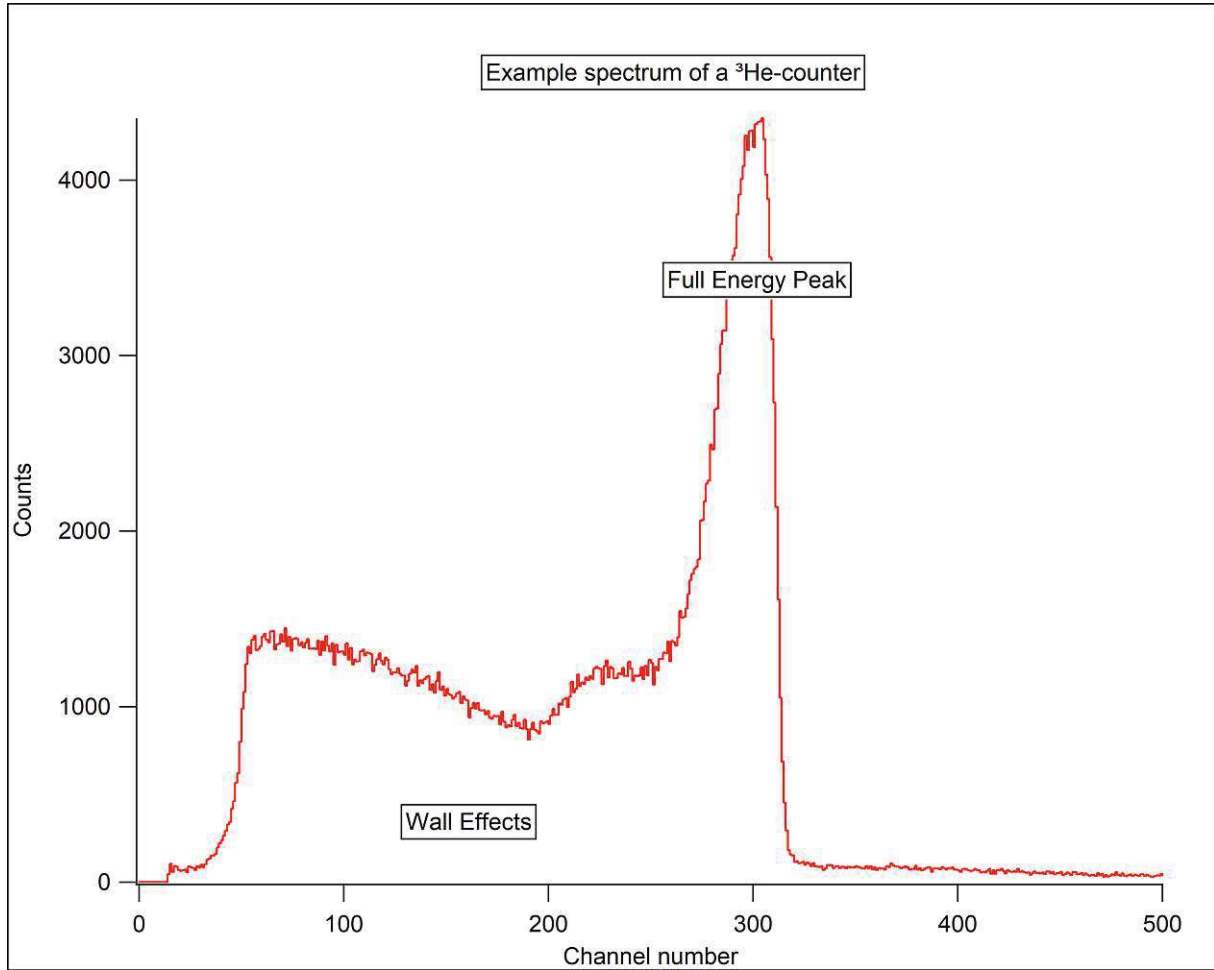


**Figure 2.3:** Example pulse height spectrum of one of the used  $^3\text{He}$ -counters

with  $m$  being the atomic mass of the detector medium. For detectors with a cuboid active volume, this information is already sufficient to determine the detector efficiency for any aperture. With a detector thickness of  $D_{\text{detector}}$ , it is calculated as

$$\varepsilon = 1 - e^{-\frac{D_{\text{detector}}\rho\sigma a}{m}} \quad (2.11)$$

Cylindrical detectors are a little bit more difficult for the path length through the detector medium depends on where the neutron impacts. The length of an arbitrary path through a cylinder with radius  $R_{\text{detector}}$  assuming a neutron beam with no divergence is calculated via the theorem of Pythagoras

$$l(y) = 2 \cdot \sqrt{R_{\text{detector}}^2 - y^2} \quad (2.12)$$

To obtain the detector efficiency, it is necessary to integrate over all allowed values of  $y$ . It runs from 0 to a maximum value of  $R_{\text{aperture}}$ . Without aperture or for apertures where width or radius are greater than or equal to the detector radius, the upper limit of

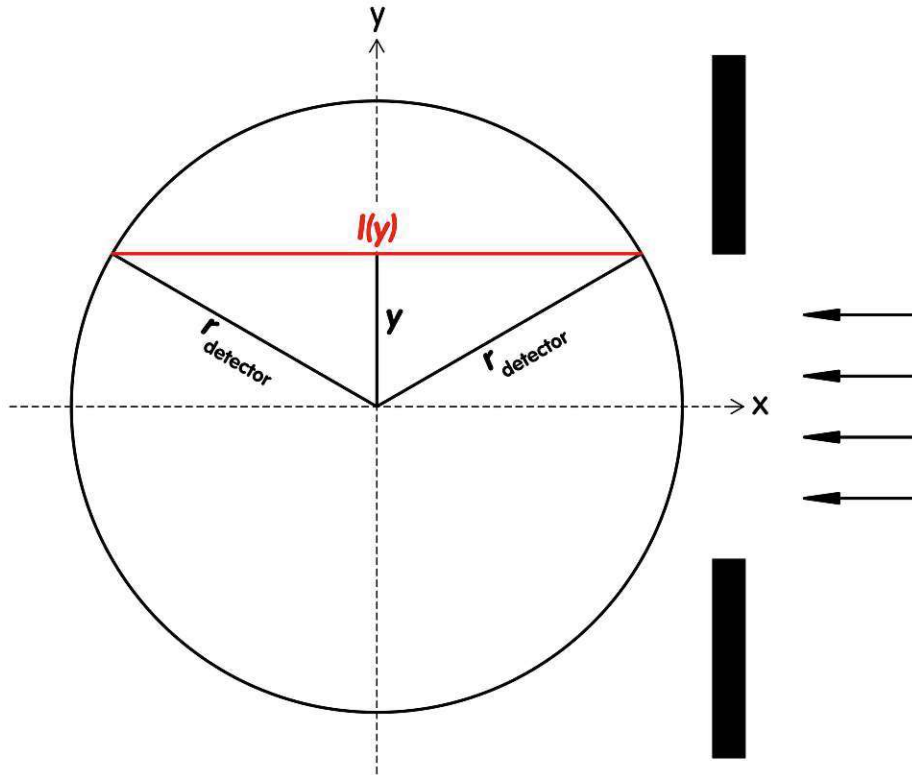


**Figure 2.4:** Sketch for calculation of the path length of neutrons through a cylindrical detector. The neutron beam comes from the right. The black rectangles portray an aperture.

the  $y$ -integration equals the detector radius. For all other configurations with rectangular apertures, it is constrained as stated in Equation 2.13:

$$\varepsilon = 1 - \frac{\int_0^{R_{\text{aperture}}} e^{-\frac{2\sqrt{R_{\text{detector}}^2 - y^2} \cdot \rho \sigma_a}{m}} dy}{R_{\text{aperture}}} \quad (2.13)$$

This will be the starting point for most calculations. For circular apertures, an additional integration has to be performed in order to account for the aperture geometry.

$$\varepsilon = 1 - \frac{\int_{z=0}^{R_{\text{aperture}}} \int_{y=0}^{y_{\text{max}}(z)} e^{-\frac{2\sqrt{R_{\text{detector}}^2 - y^2} \cdot \rho \sigma_a}{m}} dy dz}{\int_{z=0}^{R_{\text{aperture}}} \int_{y=0}^{y_{\text{max}}(z)} dy dz} \quad (2.14)$$

$$\text{with } y_{\text{max}}(z) = \sqrt{R_{\text{aperture}}^2 - z^2}$$

Additionally, it is possible to account for beam divergence via a simple estimate. This results in a correction factor of  $1/\cos(\theta)$  in the exponential function and an additional

integration  $d\theta$  from 0 to the maximum beam divergence  $\theta_{\max}$ . Applying this to Equations

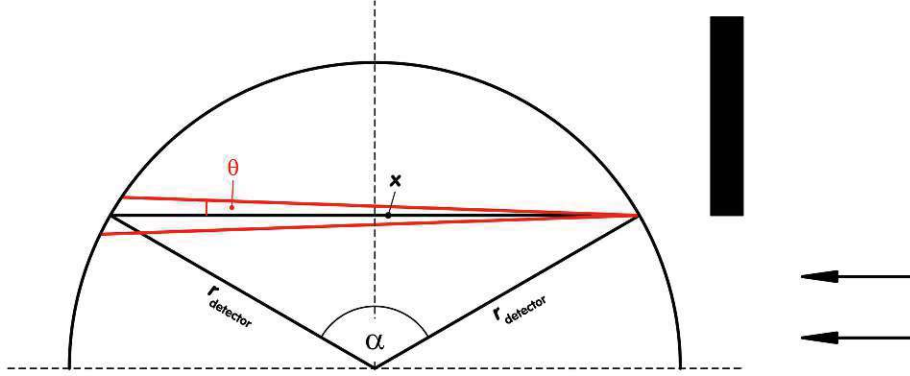


**Figure 2.5:** Sketch for deriving the correction factor necessary to account for divergence. The neutron beam comes from the right. The black rectangle portrays an aperture.

(2.13) and (2.14) yields

$$\varepsilon = 1 - \frac{\int_0^{\theta_{\max}} \int_0^{R_{\text{aperture}}} e^{-\frac{2\sqrt{R_{\text{detector}}^2 - y^2} \cdot \rho \sigma_a}{m \cos \theta}} dy d\theta}{\int_0^{\theta_{\max}} R_{\text{aperture}} d\theta} \quad (2.15)$$

$$\varepsilon = 1 - \frac{\int_0^{\theta_{\max}} \int_{z=0}^{R_{\text{aperture}}} \int_{y=0}^{y_{\max}(z)} e^{-\frac{2\sqrt{R_{\text{detector}}^2 - y^2} \cdot \rho \sigma_a}{m \cos \theta}} dy dz d\theta}{\int_0^{\theta_{\max}} \int_{z=0}^{R_{\text{aperture}}} \int_{y=0}^{y_{\max}(z)} dy dz d\theta}$$

This approximation is perfectly valid for cuboid active detector volumes. For the cylindrical case it is not perfectly correct. However, accounting for this improves the calculation by a negligible amount assuming a small beam divergence. As the divergence of a beam typically is relatively small, the additions in Equation (2.15) should generally not cause larger deviations from Equations (2.13) and (2.14).

All equations derived so far, however, assume a monochromatic neutron beam as in general, the absorption cross section  $\sigma_a$  is energy dependent. To accommodate for neutron beams with multiple discrete energies, it is easiest to calculate the efficiencies separately for each energy and then weight them according to the relative fractions each energy makes up. Alternatively one could calculate a weighted average absorption cross section and continue with the monoenergetic assumption but this method seems less true to the actual situation. In case of a neutron beam with a continuous energy spectrum,  $\sigma_a(E)$  would be used and an additional integration over the energy spectrum would be necessary. For thermal neutrons, the absorption cross section is inversely proportional to the neutron speed [18].

$$\sigma_a = \frac{\kappa}{v} \quad (2.16)$$

With this relation,  $\kappa$  being a proportionality constant, it is possible to calculate the absorption cross sections for neutrons with different energies under the constraint that they still can be considered as thermal or epithermal neutrons. With a known absorption cross section  $\sigma_{a,1}$  for neutrons with a speed of  $v_1$ , we can now calculate the cross section of neutrons with the speed of  $v_2$ :

$$\sigma_{a,2} = \sigma_{a,1} \cdot \frac{v_1}{v_2} \quad (2.17)$$

## 3 Material an Methods

### 3.1 Measurement setup

Detailed descriptions of all performed experiments are listed below, followed by details about the used detectors and Software.

#### 3.1.1 Neutron time-of-flight measurements

In order to perform the time-of-flight measurements, a chopper (Figure 3.1) was placed in the neutron beam. It consists of a cylinder rotating at a frequency of 50 Hz (resulting

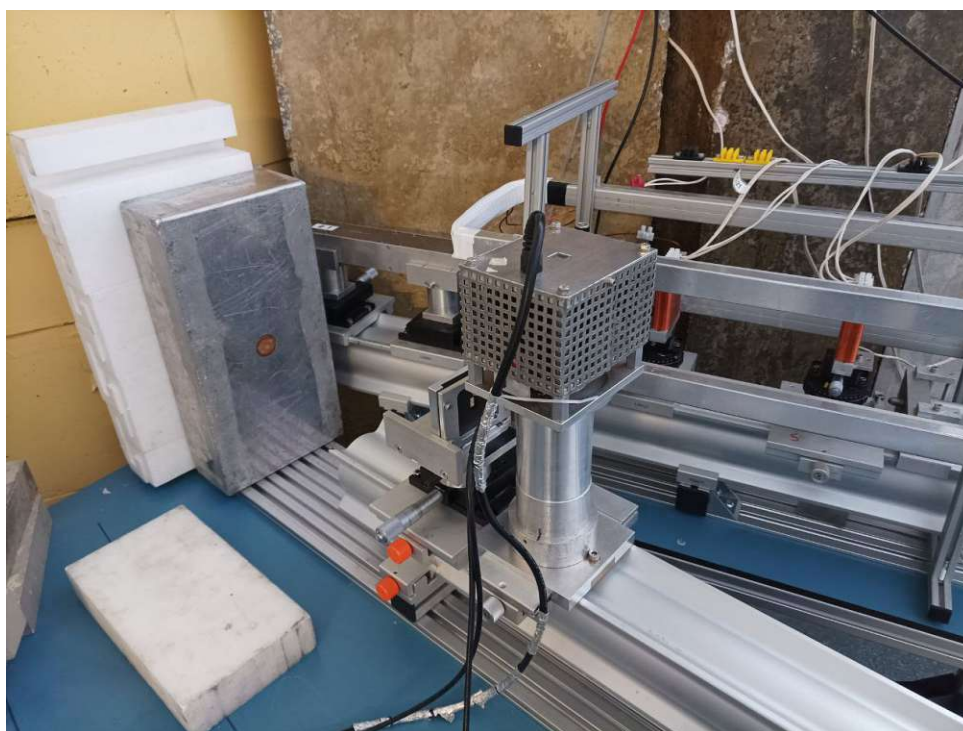


**Figure 3.1:** Chopper used for neutron time-of-flight measurements.

in an opening frequency of 100 Hz). The rotating cylinder is made of two halves of a material impermeable for neutrons. Between those two halves is a narrow layer consisting of a material transparent for neutrons, creating a channel for neutrons. Ultimately, while the chopper is in operation and rotates, neutrons can only pass while the channel is parallel to the beam axis, else all neutrons are absorbed by the cylinder. This creates a pulsed neutron beam. Behind the chopper, a  $^3\text{He}$  neutron detector is set up in variable distances, as the goal of the measurement is to measure the necessary travel times for different lengths. The needed travel time is measured as a  $\Delta t$  between the opening of the chopper channel and the detection of a neutron pulse. The used chopper has a built-in photoelectric barrier which produces a signal every time the chopper is in an "open" position allowing neutrons to pass. For obtaining  $\Delta t$ , a precise digital clock measures the

time difference between the signal from the photoelectric barrier and the signal from the neutron pulse. Measurement data is recorded in the shape of a histogram with  $\Delta t$  on the x-axis and the number of counted neutrons on the y-axis. A Gaussian fit can be laid over each created histogram, the maximum represents the mean neutron speed of the neutron beam. With increasing distance  $\Delta x$  between chopper and detector, increasing mean travel times are expected. If multiple wavelengths of neutrons are present, for larger distances  $\Delta x$  multiple peaks are expected. It has to be considered that an unwanted side effect of the chopper is a strong attenuation of the neutron beam. To account for the resulting reduction in count rates, the measurements need to be performed over longer times, typically between 10 and 20 min. A low amount of total counts would result in a relatively high statistical uncertainty, which is generally something to be avoided. Measurements were taken both with a VacuTec type 70 063 and a Canberra 20NH20/1TP in order to compare the widths of the obtained peaks and additionally analyse the effect of detector dimensions on them. Chosen measurement distances  $\Delta x$  between chopper and detector are: 10 cm, 100 cm, 150 cm and 230 cm. With the Canberra 20NH20/1TP, an additional measurement at 200 cm was taken. Larger distances between chopper and detector were not possible due to the space limitations of the beam line.

### 3.1.2 Neutron activation analysis

Before performing any measurements, the expected gamma counts for the different lines were estimated using dummy parameters. This measure was taken to get a relation for the expected values because test measurements showed extremely low count rates even though the activation process took place for more than three half-lives of  $^{116}\text{In}$ . Over a test measurement duration of 2400 s only a few hundred gamma events were registered for the major transitions.

In order to detect a relevant  $\gamma$ -photon, a few things must happen. Firstly, an incoming neutron has to be captured by an  $^{115}\text{In}$  atom and turn it into an  $^{116}\text{In}$ . The total thermal neutron absorption cross section of  $^{115}\text{In}$  is 202 b, leading to three possible excited  $^{116}\text{In}$ -states: The  $8^-$ -state, the  $5^+$ -state and the  $1^+$ -state. Of those three, the  $1^+$ -state decays with a half-life of 14.2 s into  $^{116}\text{Sn}$ . Due to its short half life, the gammas emitted by this decay can not be detected in this measurement, because the time between activation and gamma readout is over 20 half lives. The fraction of the absorption cross-section leading to this specific decay channel is about 40 b. The remaining 162.3 b are split into one channel directly leading to the  $5^+$ -state with 54.29 min half life and another channel leading to the  $8^-$ -state with a half life of 2.1 s. The  $8^-$ -state decays into the  $5^+$ -state, additionally populating it. Due to the short half-life, this transition is also unobservable in this experiment. As a result, the signal picked up by the gamma detector is purely from the  $5^+$ -state.

The probability that an incoming neutron is absorbed by a sample with thickness  $d$

is calculated as

$$\varepsilon = 1 - e^{-\frac{x\rho\sigma_a}{m_{\text{In}}}}. \quad (3.1)$$

The sample thickness can easily be derived, as surface area, mass and density are known. The total indium foil weighs 0.3438 g and has a radius of 0.01 m. The density of In is 7310 kg/m<sup>3</sup>. This leads to a thickness  $x$  of  $1.467 \cdot 10^{-4}$  m.  $m_{\text{In}} = 114.904$  u for <sup>115</sup>In. With those values, equation (3.1) leads to an absorption probability of 8.889%. The natural abundance of <sup>115</sup>In is only 95%. Furthermore, each characteristic  $\gamma$  only have a certain probability of occurring. The detector used to detect said photons also has a certain energy dependant efficiency for detecting the gammas. The corresponding values for the major five energies can be found in the table below. The probability that an impacting neutron creates a  $\gamma$  of said energies and then is detected is calculated as a product of all aforementioned probabilities and is also tabulated in table 3.1.

$E_\gamma$ [keV]	$I_\gamma(E_\gamma)$ [%]	Detector efficiency [%]	Detection probability [%]
416	27.7	0.8779	0.0207
1097	56.2	0.3338	0.0160
1293	84.4	0.3073	0.0221
1507	10.0	0.2937	0.0025
2112	15.5	0.2833	0.0037

**Table 3.1:** Probabilities for detecting characteristic gamma caused by a neutron. Detection probability is the product of absorption probability, natural abundance of <sup>115</sup>In, line probability and detector efficiency.

In addition, it is important to consider the probability of an activated Indium (<sup>116</sup>In) surviving the activation process. The average survival probability is given as

$$\frac{\int_0^{t_{\text{act}}} e^{-\lambda t} dt}{t_{\text{act}}} \quad (3.2)$$

with  $\lambda = \ln 2/t_{1/2}$  being the decay constant and  $t_{1/2}$  the halflife of <sup>116</sup>In. Activation was performed for  $t_{\text{act}} = 10\,800$  s Assuming an incoming flux of  $10^4 \text{ cm}^{-2} \text{ s}^{-1}$  and considering the 25 mm<sup>2</sup> aperture, we expect about a few hundred counts for each line. Assuming a more realistic flux of  $2.5 \cdot 10^3 \text{ cm}^{-2} \text{ s}^{-1}$  for the measurement position, 20 counts are expected for the lowest detection probability line (1507 keV) and 181 counts are expected for the highest detection probability line (1293 keV).

The neutron activation analysis was performed in a similar fashion to the following measurements with the gas proportional counters in order to ensure ideal comparability of the obtained values. The distance between the reactor wall and the Indium probe was 150 cm. An absorber block made of borated polyethylene with the double 5 mm  $\times$  5 mm aperture was used as well, ensuring a well-defined illuminated spot on the probe. A special mount

(Figure 3.2) for the Indium probe was made so it was perfectly positioned in the beam.



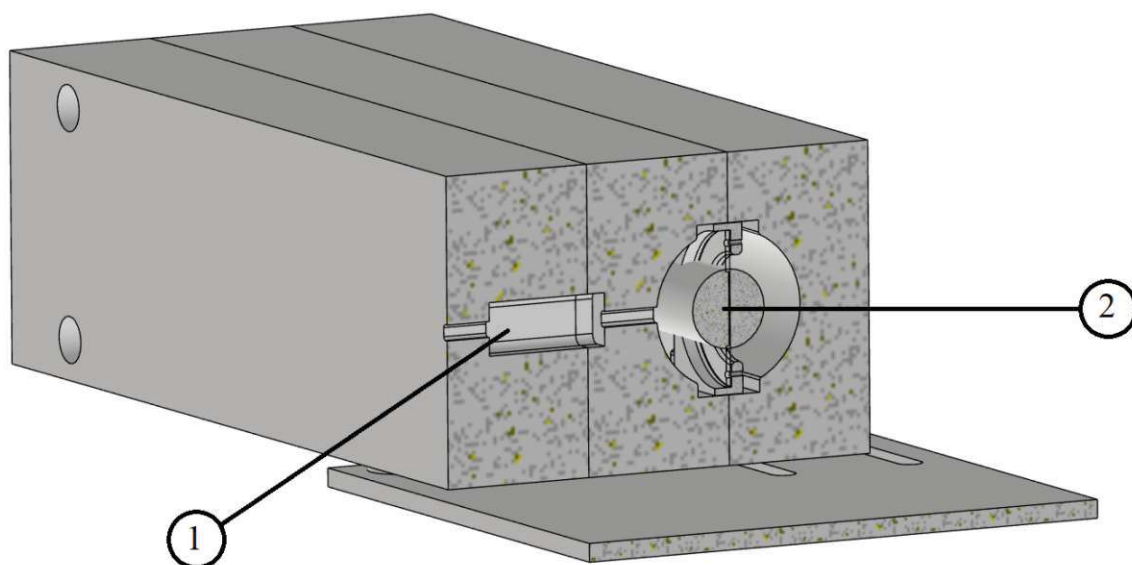
**Figure 3.2:** Mount for the Indium probes.

The used Indium itself were thin foils with masses of 0.3504 g and 0.3630 g and a radius of 1 cm. The resulting surface of the probe is substantially larger than the illuminated spot created by the 5 mm × 5 mm apertures, which made small errors with placing the probe a non-existent problem due to the size difference. The Indium was clenched between two circular acrylic glass discs; the one facing the neutron beam had a window with a diameter of 1.5 cm at its center so the neutron beam could reach the probe material unattenuated. On the rear side of the probe, a Cadmium plate was placed between the Indium and the acrylic glass. The Cadmium with its high absorption cross section for thermal neutrons reduced eventual backscattering from the second acrylic glass plate which would otherwise artificially increase the flux measured by neutron activation analysis. After the activation process, the required gamma spectra were measured with a silicon-based semiconductor detector. The sample was placed in a distance of 5 cm to the detector. The energy- and geometry-dependant efficiencies of the gamma detector were determined using reference values from calibration sources and creating a fit in order to be able to obtain the efficiencies for the relevant gamma energies. The obtained spectra were then evaluated with the on-site software of the gamma-detector, the open-source software InterSpec [19] and manually. For a brief summary of the features of InterSpec, see subsection 3.3. Evaluation was carried out following subsection 2.2

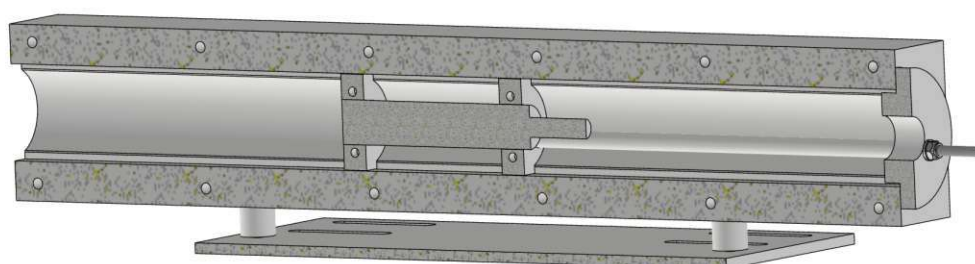
### 3.1.3 Measuring with different gas proportional counters

For determining the detector efficiency, each detector was used to take a total of 12 measurements with a duration of 60 s. The detectors were positioned in the neutron beam, the distance between the reactor wall and the detector center was 150 cm for all measurements. In order to ensure that every neutron counted actually comes from the neutron beam, the detectors were placed inside a chunk of borated polyethylene which

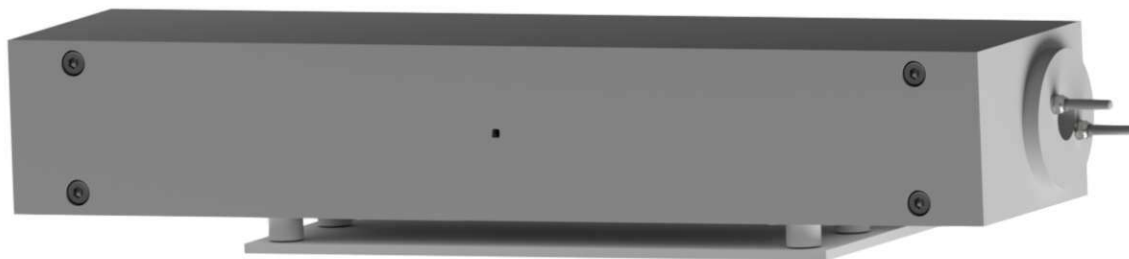
absorbed every neutron that could eventually reach the detector via scattering from other experiments or the walls of the reactor hall. The only way for neutrons to reach the detector was a set of two  $5\text{ mm} \times 5\text{ mm}$  apertures which were  $7.5\text{ cm}$  apart. This setup was chosen to reduce the effect of the beam divergence. A detailed view of the detector mount is shown in Figure 3.3. Additionally the detector mounts which were inserted in the absorbing casing were designed to position each detector in a way that the incoming beam illuminates the center of the active region of each detector.



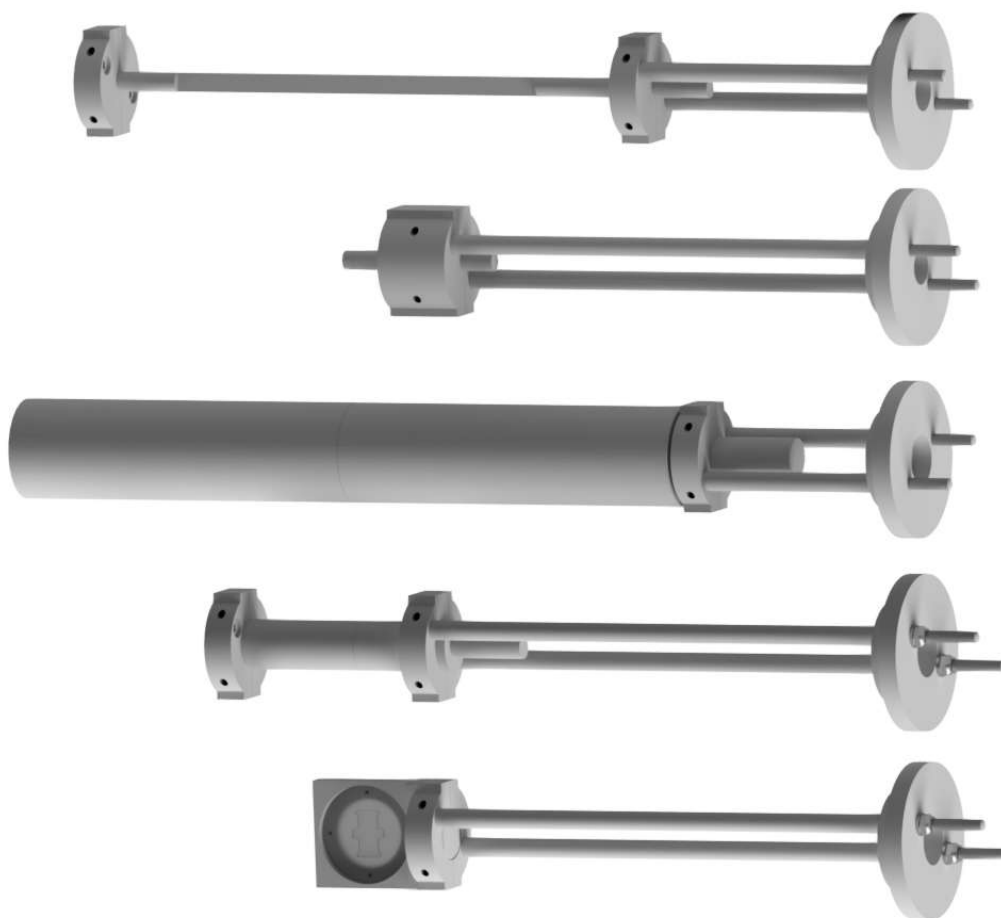
(a) Borated polyethylene casing with aperture geometry (1) and detector position (2).



(b) Positioning of the detectors within the borated polyethylene casing.



(c) Frontal view of the borated polyethylene casing with inserted detector.



(d) Individual detectors with mounts.

**Figure 3.3:** Construction design of the detector mount. Designed by Roman Gergen. Fabrication: Atominstitut Workshop.

Two sets of 6 measurements were taken with each detector in order to get somewhat statistically representative results. A detailed overview over all used neutron detectors is given in subsection 3.2. Evaluation was performed manually due to the relatively low amount of data produced. The on-site setup can be seen in Figure 3.4.

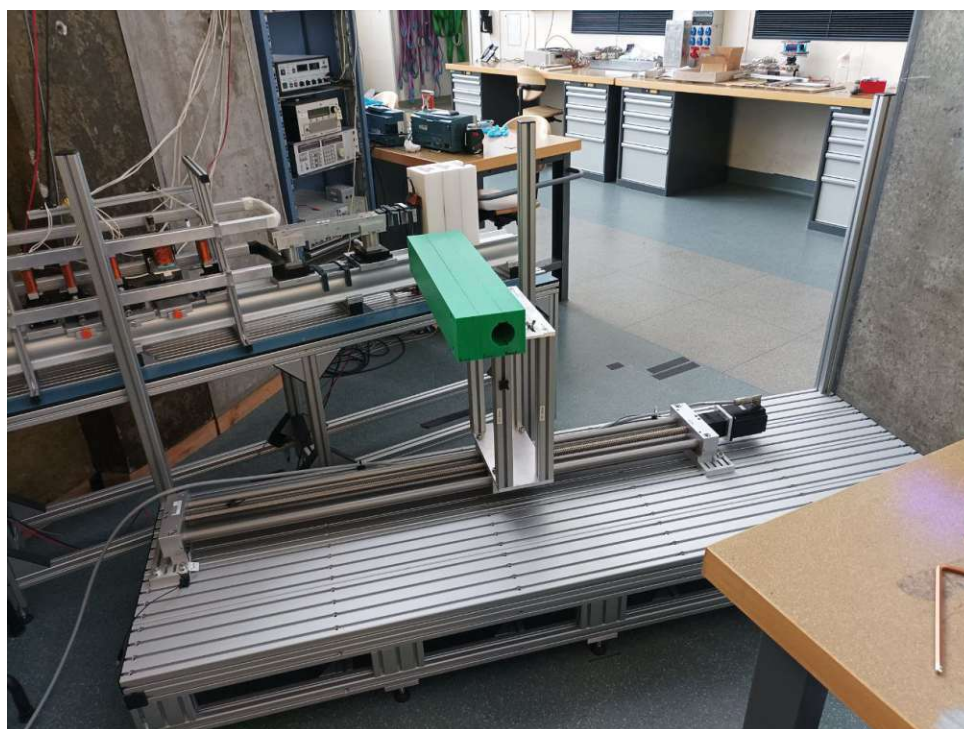


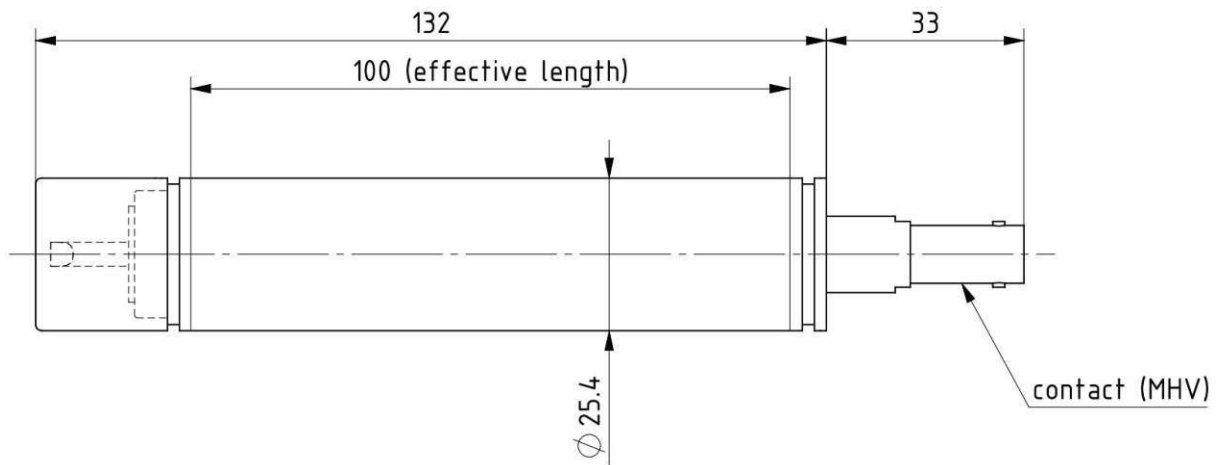
Figure 3.4: Borated polyethylene detector holder without inserted detector.

## 3.2 Utilized neutron detectors

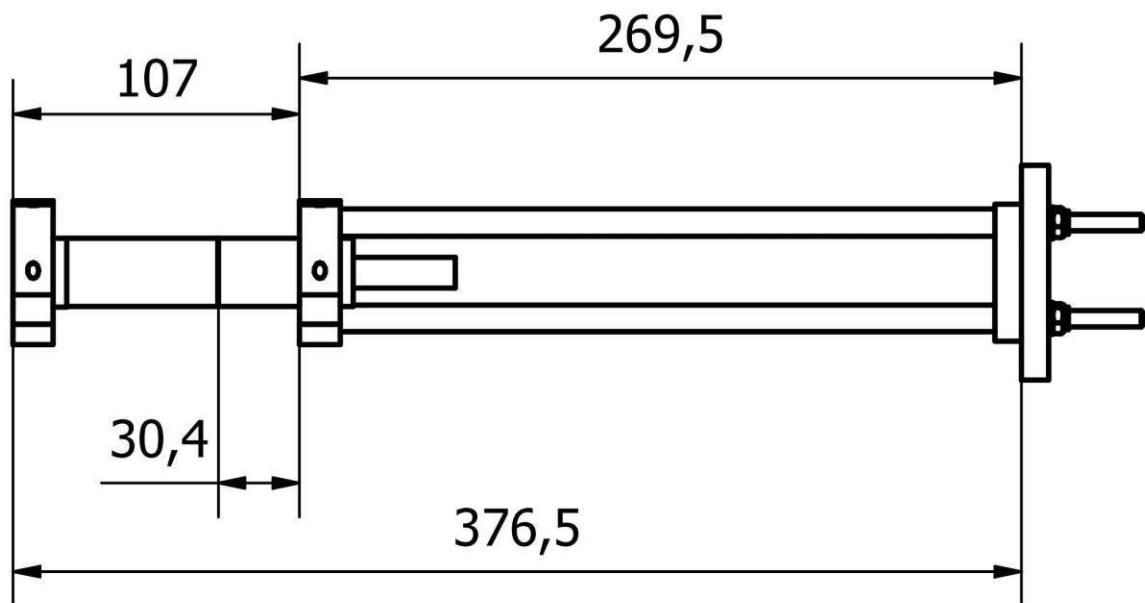
A brief overview over the various gas proportional counters will be given below. Particle densities were obtained via the pressures given by the corresponding data sheets from VacuTec [20] and Canberra [21].  $^3\text{He}$  mass- and particle densities were then calculated using the ideal gas equation. In order to obtain the  $\text{BF}_3$  mass- and particle density, the van der Waals equation was applied using the van-der-Waals parameters  $a = 3.981^2/\text{mol}^2$  and  $b = 0.54431/\text{mol}$  [22]. This didn't seem necessary for the helium, as it is a monoatomic noble gas. Boron trifluoride however, being a larger molecule, shows stronger diversions from the ideal gas model and therefore shouldn't be treated as such. The actually used operating voltages were manually determined with the help of an oscilloscope and chosen to give the best possible results.

### 3.2.1 VacuTec Type 70 063

Three identical devices of this build were used in order to test the consistency and reliability of this detector type. A technical drawing of the detector without and with mount can be seen in Figure 3.5a and 3.5b and an image of one of the used detectors with mount in Figure 3.5c. The technical data is displayed in Table 3.2.



(a) Dimensions of the VacuTec 70 063  $^3\text{He}$  detectors. Lengths are given in mm. "Effective length" refers to the length of the active volume [20].



(b) Sketch of the VacuTec 70 063  $^3\text{He}$  detector with mount. Lengths are given in mm.



(c) Image of one of the three used VacuTec 70 063  $^3\text{He}$  detectors with mount.

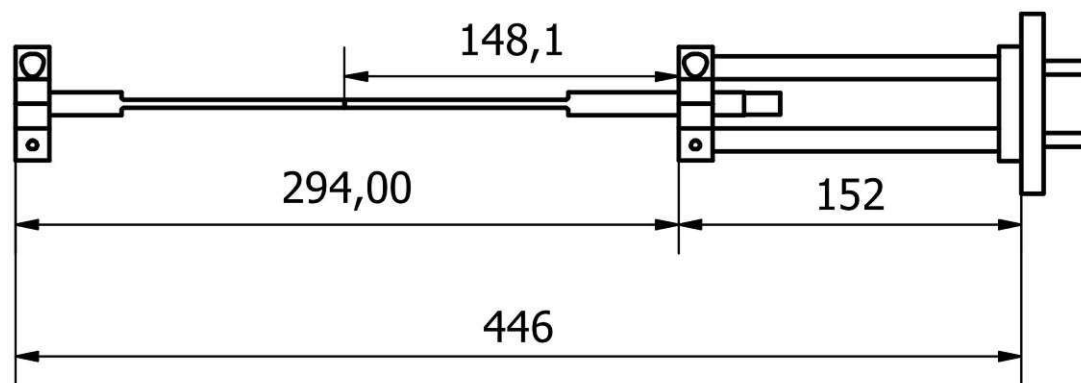
**Figure 3.5:** The VacuTec 70 063  $^3\text{He}$  detector

Nominal operating voltage	760 V
$^3\text{He}$ -pressure	4 bar $\hat{=}$ $4 \cdot 10^5$ Pa
corresponding particle density	$9.883 \cdot 10^{25} \text{ m}^{-3}$
corresponding mass density	$0.495 \text{ kg/m}^3$
Active Volume	cylindrical, $35\,230 \text{ mm}^3$
$\sigma_a(2.639 \text{ \AA})$	7824 b
$\Sigma_a(2.639 \text{ \AA})$	$77.325 \text{ m}^{-1}$
$\sigma_a(1.233 \text{ \AA})$	3654 b
$\Sigma_a(1.233 \text{ \AA})$	$36.112 \text{ m}^{-1}$
$\sigma_a(0.822 \text{ \AA})$	2390 b
$\Sigma_a(0.822 \text{ \AA})$	$23.620 \text{ m}^{-1}$
Expected thermal efficiency	66.91%
Manufacturer sensitivity	$40.6 \pm 4\%$

**Table 3.2:** Operating parameters of the VacuTec 70 063  $^3\text{He}$  detector. Nominal operating voltage,  $^3\text{He}$ -pressure, active volume and Manufacturer sensitivity were taken or calculated from [20].

### 3.2.2 Canberra 20NH20/1TP

Two identical devices of this build were used in order to test the consistency and reliability of this detector type. A sketch and an image of the Canberra 20NH20/1TP  $^3\text{He}$  counter can be found in Figure 3.6, the technical data is displayed in Table 3.3. The entire active region is located in the squashed section of the detector, the other regions do not contribute to it.



(a) Sketch of the Canberra 20NH20/1TP  $^3\text{He}$  detector with mount. Lengths are given in mm.



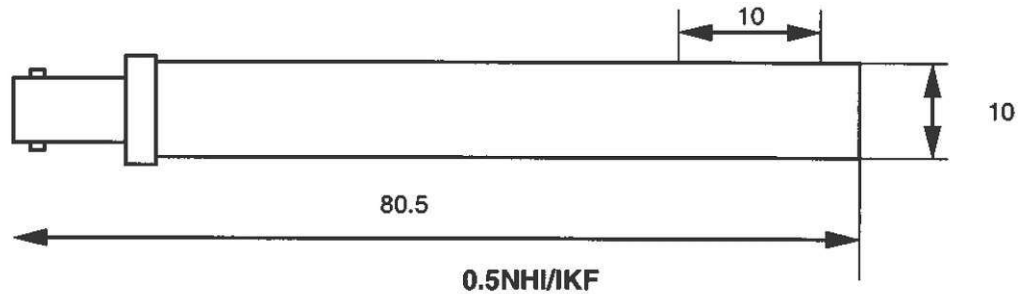
(b) Image of one of the two used Canberra 20NH20/1TP  $^3\text{He}$  detectors with mount.

**Figure 3.6:** The Canberra 20NH20/1TP  $^3\text{He}$  detector.

Nominal operating voltage	1700 V
Used operating voltage	1640 V
$^3\text{He}$ -pressure	20 bar $\approx 2 \cdot 10^6$ Pa
corresponding particle density	$4.941 \cdot 10^{26} \text{ m}^{-3}$
corresponding mass density	$2.475 \text{ kg/m}^3$
Active length	200 mm
Active section	$2.5 \text{ mm} \times 13.5 \text{ mm}$
Active Volume	cuboid, $6750 \text{ mm}^3$
$\sigma_a(2.639 \text{ \AA})$	7824 b
$\Sigma_a(2.639 \text{ \AA})$	$386.584 \text{ m}^{-1}$
$\sigma_a(1.233 \text{ \AA})$	3654 b
$\Sigma_a(1.233 \text{ \AA})$	$180.544 \text{ m}^{-1}$
$\sigma_a(0.822 \text{ \AA})$	2390 b
$\Sigma_a(0.822 \text{ \AA})$	$118.090 \text{ m}^{-1}$
Expected thermal efficiency	48.25%
Manufacturer sensitivity	48% at $1.8 \text{ \AA}$

**Table 3.3:** Operating parameters of the Canberra 20NH20/1TP  $^3\text{He}$  detector. Nominal operating voltage,  $^3\text{He}$ -pressure, active length and section were taken or calculated from [21]

## 3.2.3 Canberra 0.5NH1/1KF

(a) Dimensions of the Canberra 0.5NH1/1KF  $^3\text{He}$  detector. Lengths are given in mm [21].(b) Sketch of the Canberra 0.5NH1/1KF  $^3\text{He}$  detector with mount. Lengths are given in mm.(c) Image of the Canberra 0.5NH1/1KF  $^3\text{He}$  detector with mount.**Figure 3.7:** The Canberra 0.5NH1/1KF  $^3\text{He}$  detector.

A technical drawing of the detector can be seen in Figure 3.7a and an image of one of the used detector in Figure 3.7c. The technical data is displayed in Table 3.2. The datasheet does not provide information about the wall thickness of this detector. As the outer diameter is 10 mm, this can not possibly be the diameter of the active volume. To confirm this, an image of the detector was taken via neutron radiography (Figure 3.8).

Nominal operating voltage	1600 V
Used operating voltage	1460 V
$^3\text{He}$ -pressure	8 bar $\approx 8 \cdot 10^5$ Pa
corresponding particle density	$1.977 \cdot 10^{26} \text{ m}^{-3}$
corresponding mass density	0.990 kg/m <sup>3</sup>
Active Volume	cylindrical, 785 mm <sup>3</sup>
$\sigma_a(2.639 \text{ \AA})$	7824 b
$\Sigma_a(2.639 \text{ \AA})$	154.680 m <sup>-1</sup>
$\sigma_a(1.233 \text{ \AA})$	3654 b
$\Sigma_a(1.233 \text{ \AA})$	72.240 m <sup>-1</sup>
$\sigma_a(0.822 \text{ \AA})$	2390 b
$\Sigma_a(0.822 \text{ \AA})$	47.250 m <sup>-1</sup>
Expected thermal efficiency	62.67%
Manufacturer sensitivity	50%

**Table 3.4:** Operating parameters of the Canberra 0.5NH1/1KF  $^3\text{He}$  detector. Nominal operating voltage,  $^3\text{He}$ -pressure and active volume were taken or calculated from [21]

With help of a polyethylene absorber of known size, it was possible to estimate the wall thickness from this image, resulting in a wall thickness of 0.824 mm, reducing the active volume around 550 mm<sup>3</sup>. The Radiography data allows us to furthermore differentiate between active volume and gas-filled volume. The leftmost edge of the structure on the right of the dark gray region in Figure 3.8 limits the active volume to a length of about 10 mm yet it is clearly visible that this structure does not span across the entire cylinder radius, leaving some space to be filled with  $^3\text{He}$ . The excess volume amounts about 220 mm<sup>3</sup>, resulting in a total gas filled volume of around 750 mm<sup>3</sup>. While this has an effect on the particle number, the particle density obviously stays the same.

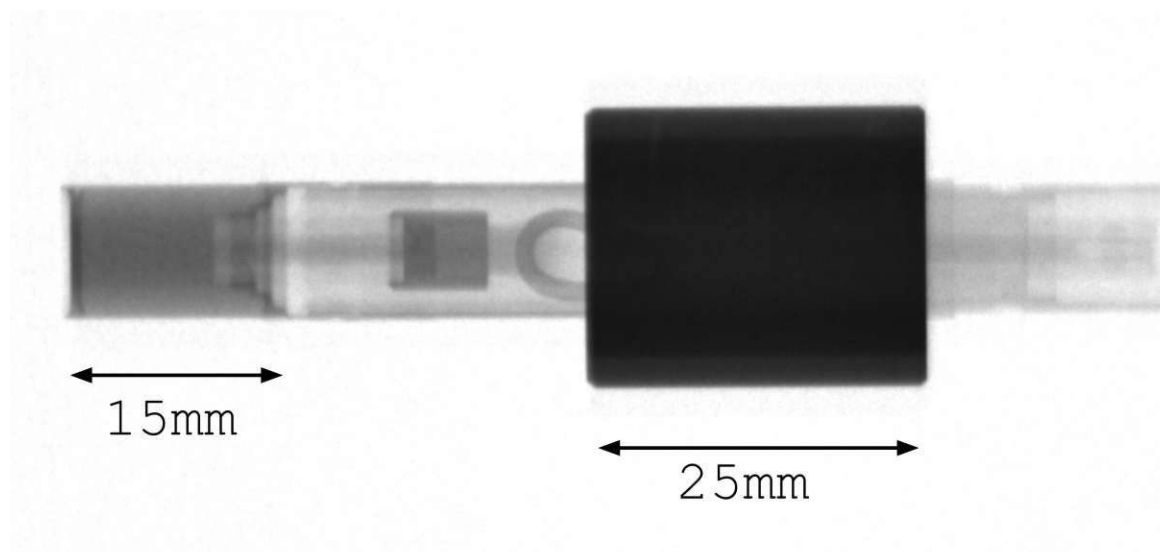
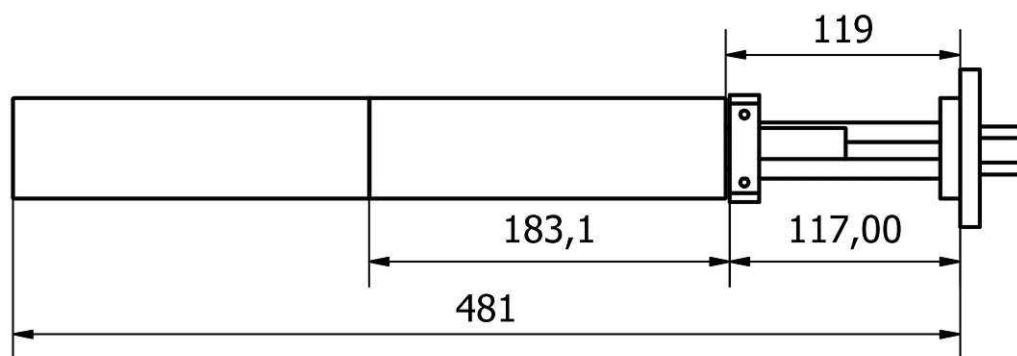


**Figure 3.8:** Neutron radiography image of the Canberra 0.5NH1/1KF  $^3\text{He}$  detector.

### 3.2.4 Reuter Stokes $\text{BF}_3$ -counter



(a) Sketch of the Reuter Stokes  $\text{BF}_3$  detector with mount. Lengths are given in mm.



(b) Image of the Reuter Stokes  $\text{BF}_3$  detector with mount.

**Figure 3.9:** Reuter Stokes  $\text{BF}_3$  counter with detector mount on the left.

A technical drawing of the detector can be seen in Figure 3.9a and an image of one of the used detector in Figure 3.9b. Due to the age of the detector, the exact model and technical

data are mostly unknown. Due to it being frequently utilized for various experiments, examining this detector type was of interest. As  $\text{BF}_3$  has only one boron atom, the particle density of the gas is identical to the boron particle density. To gather the  $^{10}\text{B}$  particle density, the enrichment has to be factored in. 96% enrichment is a commonly used value in neutron detection applications and was therefore used for the calculations.

Used operating voltage	2260 V
$\text{BF}_3$ -pressure	700 mmHg $\hat{=}$ 93 326 Pa
corresponding $\text{BF}_3$ particle density	$2.316 \cdot 10^{25} \text{ m}^{-3}$
corresponding $\text{BF}_3$ mass density	2.578 kg/m <sup>3</sup>
corresponding $^{10}\text{B}$ particle density	$2.223 \cdot 10^{25} \text{ m}^{-3}$
corresponding $^{10}\text{B}$ mass density	0.370 kg/m <sup>3</sup>
Length	350 mm
Radius	21 mm
Active Volume	cylindrical, 484 940 mm <sup>3</sup>
$\sigma_a(2.639 \text{ \AA})$	5629 b
$\Sigma_a(2.639 \text{ \AA})$	12.513 m <sup>-1</sup>
$\sigma_a(1.233 \text{ \AA})$	2629 b
$\Sigma_a(1.233 \text{ \AA})$	5.844 m <sup>-1</sup>
$\sigma_a(0.822 \text{ \AA})$	1720 b
$\Sigma_a(0.822 \text{ \AA})$	3.824 m <sup>-1</sup>
Expected thermal efficiency	29.79%

**Table 3.5:** Operating parameters of the Reuter Stokes  $\text{BF}_3$  detector.

### 3.3 Spectral radiation analysis software "InterSpec" v1.0.11

InterSpec is an open source software for evaluation of nuclear radiation spectra. It is available on GitHub [19]. Because the software itself is still being improved regularly, newer versions might already be available for use. It has the ability to read many different file formats commonly used to store spectral data in, one of them being the .cnf format our gamma detector created. The software comes with a large built-in library of reference data for many nuclides, making it especially easy to find the desired information. Furthermore it is capable of more advanced calculations in terms of e.g. shielding. Most of those features were not even necessary to acquire the simple data needed for this thesis. A brief overview over the used functions will be given below:

Firstly, loading the obtained data into the software is fairly easy as can be seen in Figure 3.10 - it provides the option to choose files as foreground or background. Loading a background in addition to a foreground later provides the option to subtract the background from the foreground, giving access to a backgroundless difference spectrum.

Once the desired spectra are loaded, the software already displays them as a graph with some additional information like total counts, detector real time and live time. Each singular spectrum can be scaled individually. Additionally, it is possible to just look at a selected energy window. To gain a better grasp of the relevant energies, it is possible to set up references for the isotope one is looking at. Figure 3.11 shows how to select the reference lines. Those are especially helpful for the following peak search, as they are excellent for orientation in the spectrum. Adding the peaks is done via the "peak manager" tab. It provides the user with the options to either manually add peaks or to utilise a peak location algorithm. Especially for peaks with low intensity it is advantageous to add them manually.

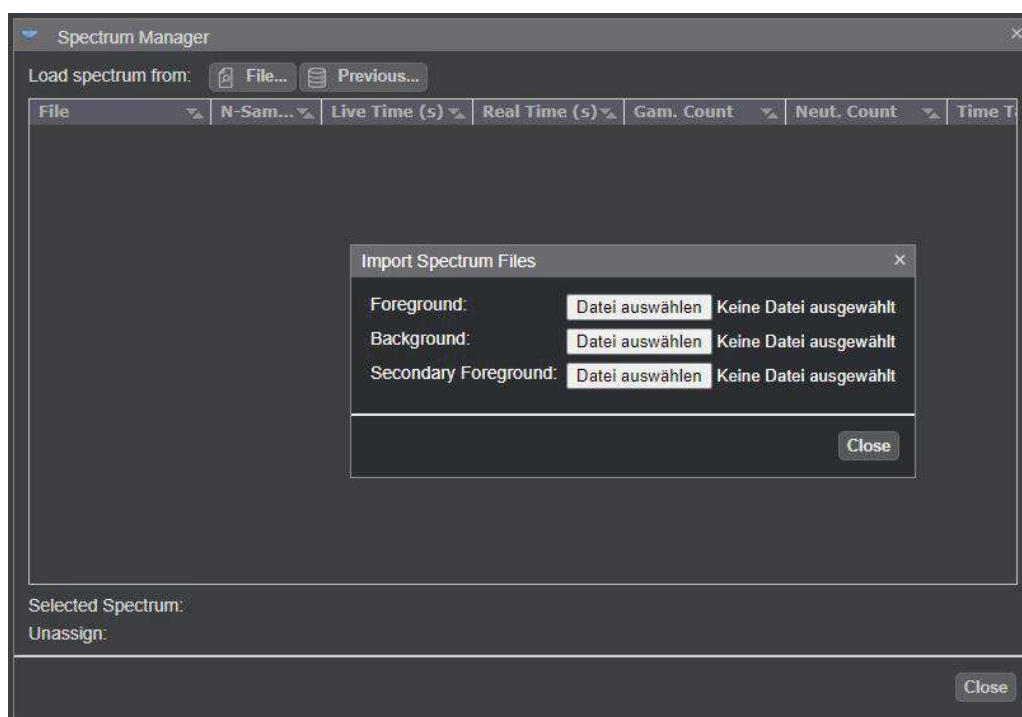


Figure 3.10: Loading spectra in InterSpec.

For pronounced peaks, the algorithm works just fine. It will probably detect some unwanted peaks from natural background radioactivity or similar naturally occurring interference. Thanks to the already set up reference photopeaks, it is fairly simple to differentiate between wanted and unwanted peaks. If the mean of a peak matches one of the reference lines, the software automatically associates it with the reference, displaying it in the colour chosen for the reference. Peaks where no reference could be found are left gray. For creating the peaks in the spectrum, one can easily untick all unwanted peaks so only relevant information is displayed and the spectrum does not become cluttered. An

example of the results of an automated peak search can be found in Figure 3.13. Finally, the spectrum with the characteristics of its peaks are displayed. (Figure 3.14)

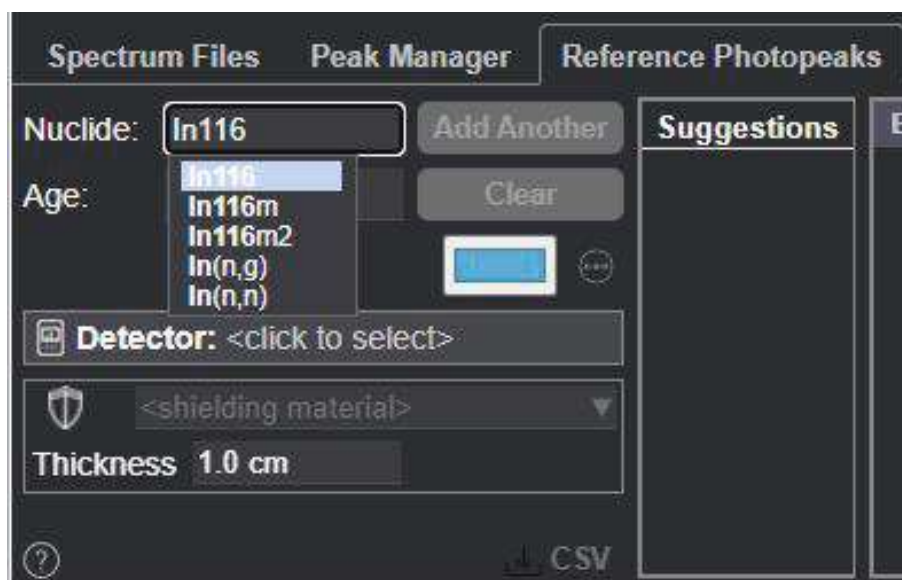


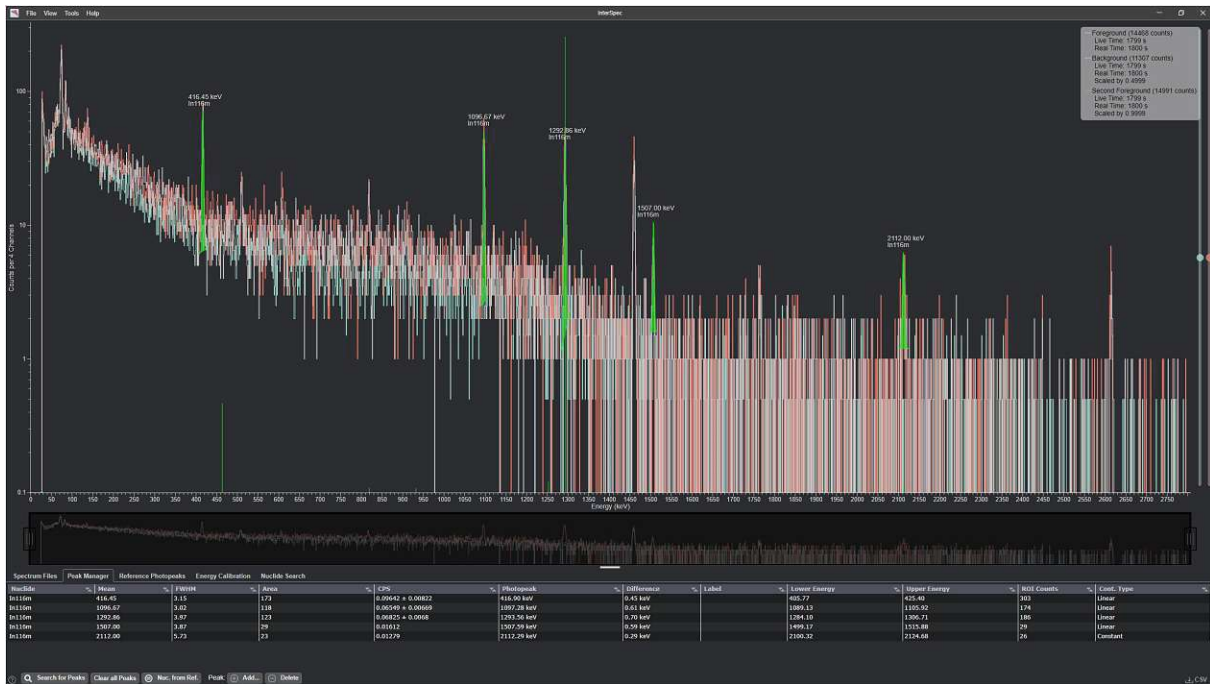
Figure 3.11: Setting up reference lines. In this case, In116m was used.



Figure 3.12: Manual addition of a peak at 1507 keV. Due to the low intensity, it is barely discernable from the background.



Figure 3.13: Results screen of the peak search algorithm. Peaks at the energies of a reference line are displayed in a chosen colour.



(a) Obtained spectrum with added peaks at relevant gamma transitions

Nuclide	Mean	FWHM	Area
In116m	416.45	3.15	173
In116m	1096.67	3.02	118
In116m	1292.86	3.97	123
In116m	1507.00	3.87	29
In116m	2112.00	5.73	23

(b) Selection of peak characteristics at the bottom left of Figure 3.14a

**Figure 3.14:** Complete obtained spectrum with peak characteristics needed for further evaluation. Foreground 1 (white) and foreground 2 (red) originate from two different measurements, the background is displayed in blue. Reference lines and the corresponding peaks in the spectrum are shown in green.

## 4 Results

### 4.1 Neutron activation analysis

A neutron activation analysis was performed on two different Indium probes:

The first probe was exposed to the neutron flux for  $t_{\text{irr}} = 10\,800\text{ s}$ . The decay time from stop of activation to start of gamma measurement was  $t_{\text{decay}} = 420\text{ s}$ . The gamma measurement had a total duration of  $t_{\text{measurement}} = 1800\text{ s}$  with a live time of  $t_{\text{live}} = 1798.6\text{ s}$ . The mass of the Indium sample was determined to be  $0.3504\text{ g}$ . The second probe was exposed to the neutron flux for  $t_{\text{irr}} = 10\,800\text{ s}$ . The decay time from stop of activation to start of gamma measurement was  $t_{\text{decay}} = 300\text{ s}$ . The gamma measurement had a total duration of  $t_{\text{measurement}} = 1800\text{ s}$  with a live time of  $t_{\text{live}} = 1798.9\text{ s}$ . The mass of the Indium sample was determined to be  $0.3630\text{ g}$ . The evaluation results can be seen in Table 4.1, 4.2 and 4.3. The errors in Table 4.1 and 4.2 were given by the used software, the errors in Table 4.3 were calculated as the square root of the total counts contributing to a peak, which is the standard deviation for poisson distributions.

Energy [keV]	Peaks 1 [cts]	Flux 1 [ $\text{cm}^{-2}\text{s}^{-1}$ ]	Peaks 2 [cts]	Flux 2 [ $\text{cm}^{-2}\text{s}^{-1}$ ]
416	$159 \pm 20$	$2370 \pm 300$	$155 \pm 26$	$2250 \pm 390$
1097	$106 \pm 20$	$2050 \pm 380$	$139 \pm 18$	$2630 \pm 330$
1293	$139 \pm 2$	$1950 \pm 30$	$157 \pm 32$	$2140 \pm 440$

**Table 4.1:** Peak areas and errors determined using the on-site software. 1 und 2 refer to the different Indium probes.

The on-site software was not able to locate the gamma peaks at  $1507\text{ keV}$  and  $2112\text{ keV}$ .

Energy [keV]	Peaks 1 [cts]	Flux 1 [ $\text{cm}^{-2}\text{s}^{-1}$ ]	Peaks 2 [cts]	Flux 2 [ $\text{cm}^{-2}\text{s}^{-1}$ ]
416	$173 \pm 15$	$2590 \pm 220$	$165 \pm 15$	$2400 \pm 210$
1097	$118 \pm 12$	$2280 \pm 230$	$136 \pm 13$	$2570 \pm 250$
1293	$123 \pm 12$	$1720 \pm 170$	$150 \pm 14$	$2050 \pm 180$
1507	$34 \pm 1$	$4200 \pm 120$	$31 \pm 1$	$3730 \pm 120$
2112	$20 \pm 1$	$1650 \pm 80$	$21 \pm 1$	$1700 \pm 80$

**Table 4.2:** Peak areas and errors determined using InterSpec. 1 und 2 refer to the different Indium probes.

Evaluation via the software InterSpec provided Peak areas for all gamma energies. The peaks at  $1507\text{ keV}$  and  $2112\text{ keV}$  had to be added manually.

Energy [keV]	Peaks 1 [cts]	Flux 1 [cm <sup>-2</sup> s <sup>-1</sup> ]	Peaks 2 [cts]	Flux 2 [cm <sup>-2</sup> s <sup>-1</sup> ]
416	149 ± 14	2220 ± 200	160 ± 14	2330 ± 200
1097	113 ± 11	2190 ± 220	147 ± 13	2780 ± 240
1293	141 ± 12	1970 ± 140	150 ± 13	2050 ± 180
1507	15 ± 5	1860 ± 570	9 ± 4	1040 ± 510
2112	10 ± 4	850 ± 300	5 ± 3	410 ± 230

**Table 4.3:** Peak areas and errors determined manually. 1 und 2 refer to the different Indium probes.

Manual evaluation was performed by gathering the channel numbers of the maximum location via InterSpec. The upper and lower limit of each peak were determined manually. The denoted errors are the square root of the total counts in one peak. Background contribution was estimated by averaging the 200 next neighbours on both sides of each peak. Using the data of table 4.7, we find a global correction factor of  $1.144 \pm 0.009$  for all determined fluxes to compensate for the monochromatic assumption. It is calculated as the quotient of the cross-section for thermal neutrons divided by the average occurring cross-section.

## 4.2 Spectral distribution of the neutron beam

The obtained data from the measurements were plotted using python. In the following graphs, the measurement data are displayed in blue. For accurate determination of the position of the maxima, Gaussian fits weighted with the standard derivation of the measured values were created (note: in order to achieve this, all channels containing a 0 had to be removed, otherwise the fit couldn't be created due to a divide by 0 error). The used fit functions were

$$\begin{aligned}
 f(t) &= M + a \cdot e^{-b \cdot (t-t_1)^2} \\
 f(t) &= M + a \cdot e^{-b \cdot (t-t_1)^2} + c \cdot e^{-d \cdot (t-t_2)^2} \\
 f(t) &= M + g \cdot e^{-h \cdot (t-t_3)^2} + a \cdot e^{-b \cdot (t-t_1)^2} + c \cdot e^{-d \cdot (t-t_2)^2}
 \end{aligned} \tag{4.1}$$

depending on the number of peaks present in the fit.  $M$  is the constant background signal, the  $t_i$  are the positions of the maxima which needed to be determined.  $a$ ,  $b$ ,  $c$ ,  $d$ ,  $g$ ,  $h$  are other fit parameters which are not needed for further evaluation. The standard deviations of the fit parameters for the locations of the maxima were at least three orders of magnitude smaller than the fit parameters and therefore neglected. Furthermore, the standard deviation of the fit parameters does not represent the statistical error of the measurements whatsoever, it only describes the fit itself. The experimental error is derived as the square root of the number of counts within a peak as the data follows a Poisson distribution.

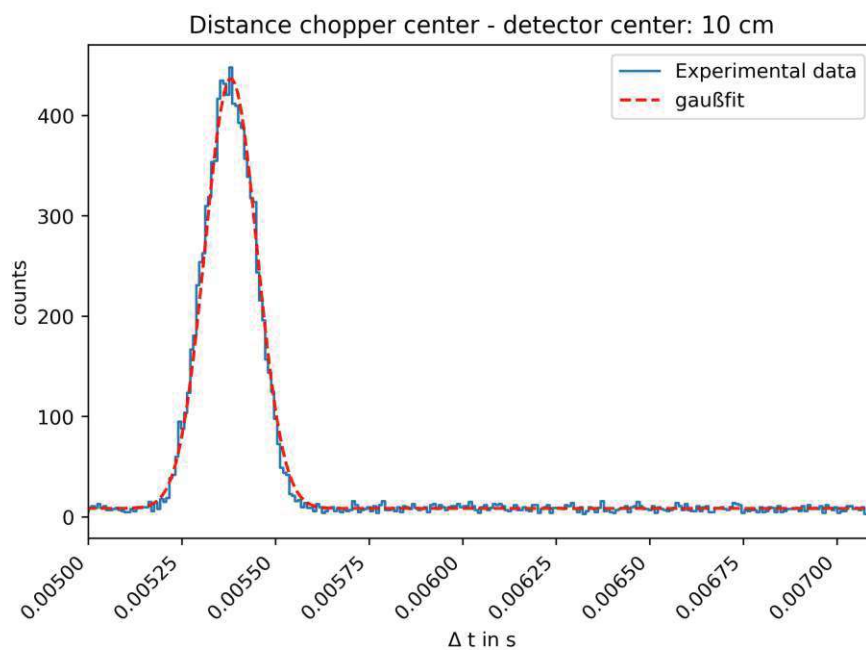
As a convention for the naming of the peaks, it was decided to define the peaks occurring starting from Figure 4.1b as peak 1 and peak 2 (corresponding to  $t_1$  and  $t_2$  from equation (4.1)). The small peak visible at higher distances between chopper and detector was then named peak 3 (corresponding to  $t_3$  from equation (4.1)). The error of the maximum

positions was calculated as the unbiased sample variance. One sample consists of one VacuTec measurement and one Canberra measurement.

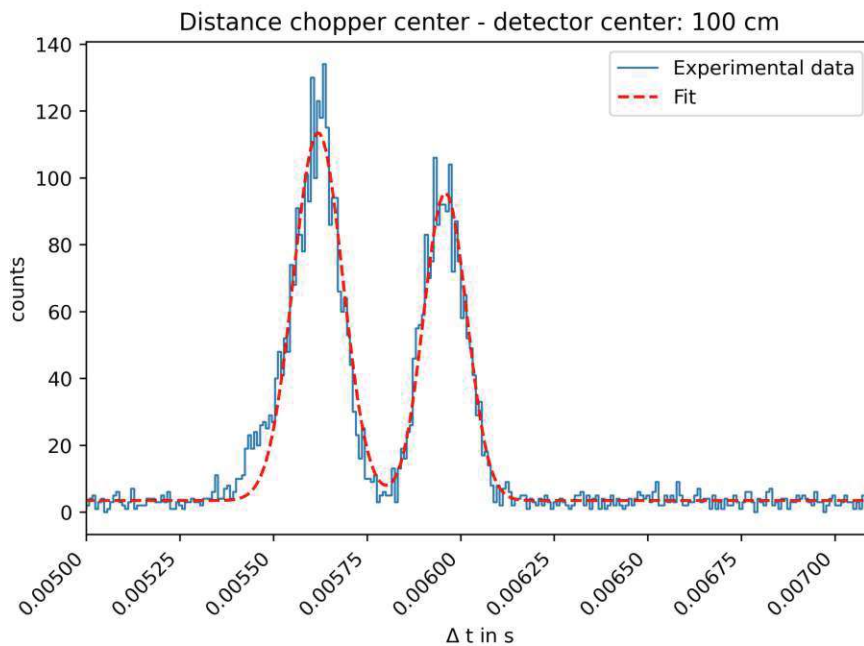
$$\sigma^2 = \frac{1}{n-1} \sum_{i=1}^n (x_i - \bar{x})^2 \quad (4.2)$$

$$\text{with } \bar{x} = \frac{1}{n} \sum_{i=1}^n x_i$$

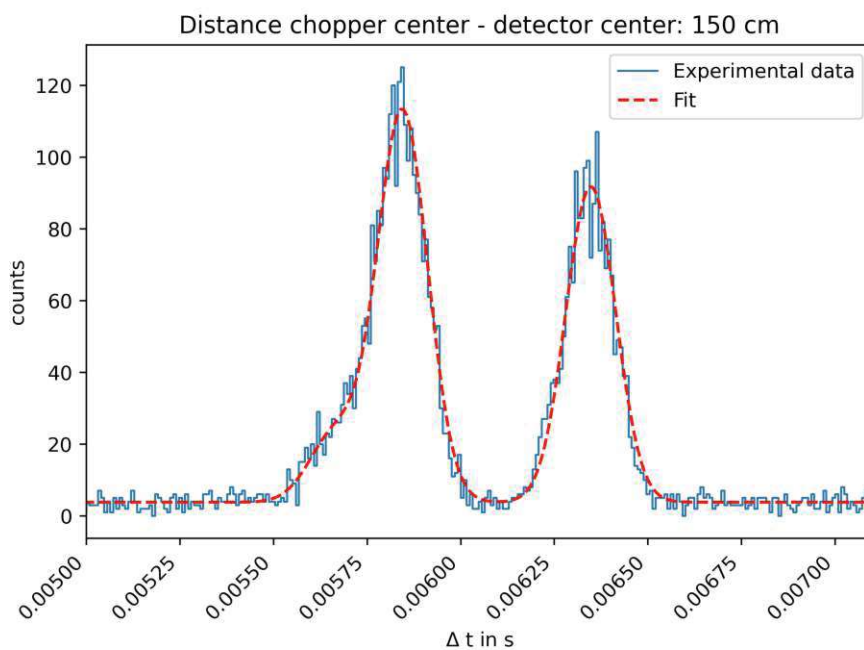
For comparison of the peak areas, the error was calculated as the square root of the total counts contributing to a peak, which is the standard deviation for poisson distributions. The first series of measurements was performed using a VacuTec Type 70 063  $^3\text{He}$  detector.



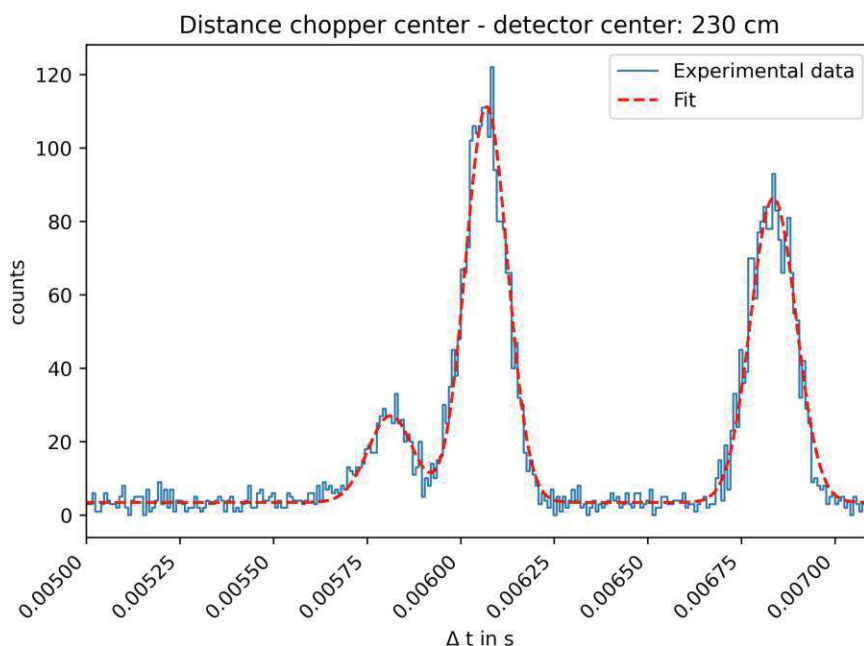
(a) Measurement data and fit for 10 cm between chopper and detector. Resulting maximum at  $t_1 = 5.384 \cdot 10^{-3} \pm 3.29 \cdot 10^{-6}$  s. Measurement duration: 10 min



(b) Measurement data and fit for 100 cm between chopper and detector. Resulting maxima at  $t_1 = 5.624 \cdot 10^{-3} \pm 8.28 \cdot 10^{-6}$  s and  $t_2 = 5.962 \cdot 10^{-3} \pm 9.47 \cdot 10^{-6}$  s. Measurement duration: 10 min



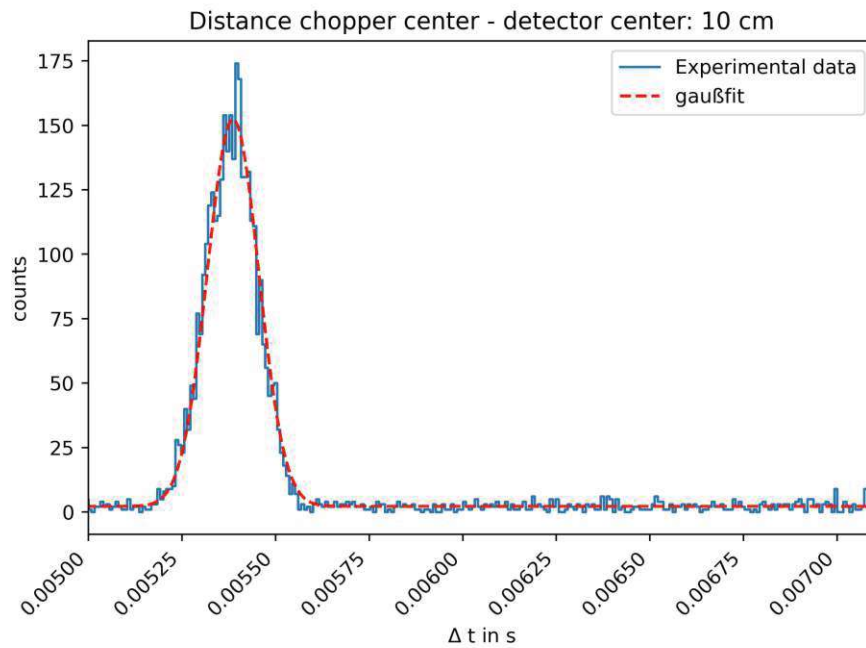
(c) Measurement data and fit for 150 cm between chopper and detector. Resulting maxima at  $t_1 = 5.840 \cdot 10^{-3} \pm 2.13 \cdot 10^{-5}$  s,  $t_2 = 6.350 \cdot 10^{-3} \pm 2.83 \cdot 10^{-5}$  s and  $t_3 = 5.675 \cdot 10^{-3} \pm 3.77 \cdot 10^{-5}$  s. Measurement duration: 15 min



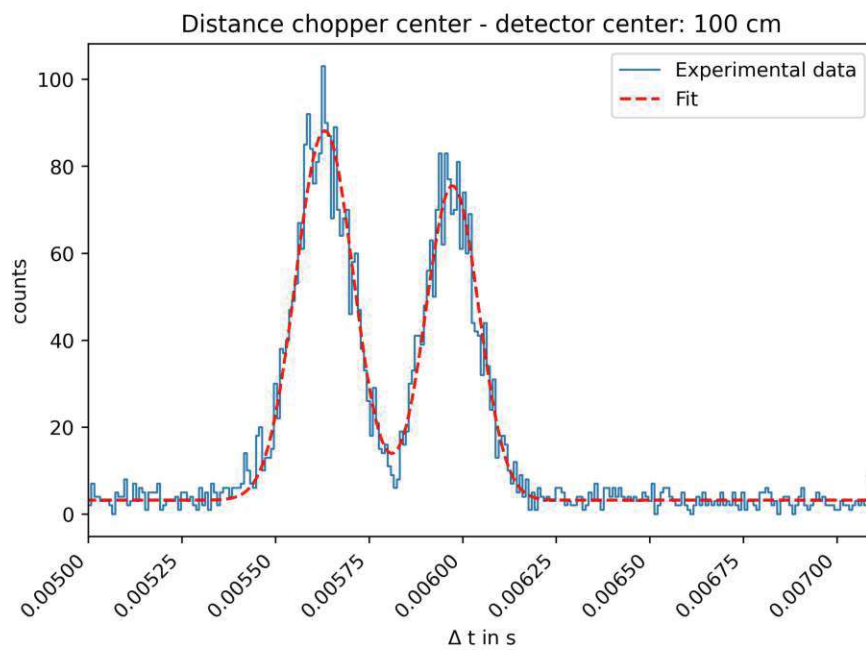
(d) Measurement data and fit for 230 cm between chopper and detector. Resulting maxima at  $t_1 = 6.072 \cdot 10^{-3} \pm 3.41 \cdot 10^{-6}$  s,  $t_2 = 6.838 \cdot 10^{-3} \pm 5.24 \cdot 10^{-6}$  s and  $t_3 = 5.818 \cdot 10^{-3} \pm 1.06 \cdot 10^{-5}$  s. Measurement duration: 20 min

**Figure 4.1:** Collected measurement data from the n-TOF measurements performed with the VacuTec Type 70 063  $^3\text{He}$  detector.

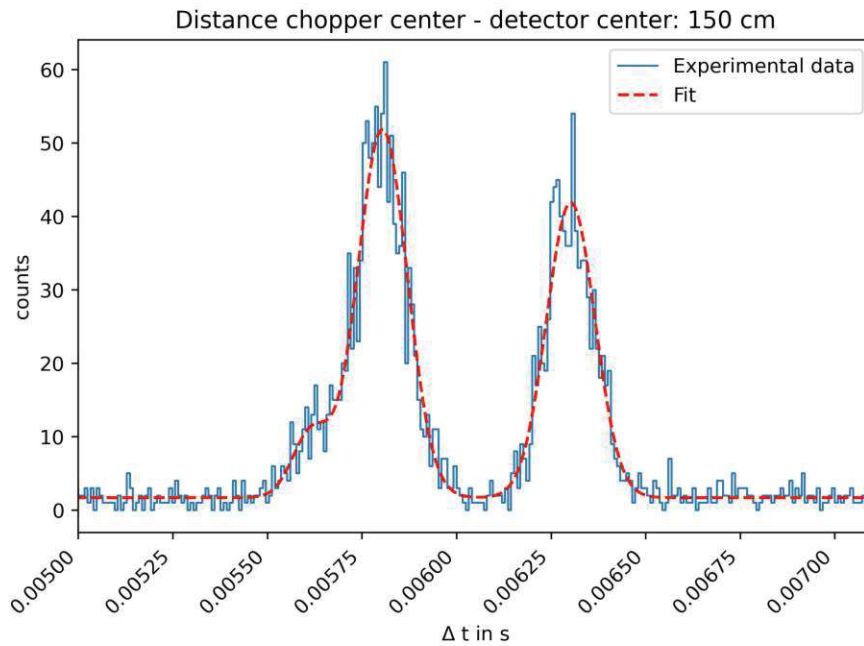
For consistency same measurements were then repeated with a Canberra 20NH20/1TP  $^3\text{He}$  detector. One additional measurement was taken at a distance of 200 cm between chopper and detector in order to create enough data to determine the speed related to the third peak. The expectancy was furthermore that the peaks width would be smaller due to the shorter path length of the neutrons in the detector which results in a strongly reduced position uncertainty of the neutron detection. While in theory this should have an impact on peak width, this is in fact barely noticeable. With flight distances of 10 cm upwards, an uncertainty of about  $\pm 1$  cm distorts the flight distance by 10% at worst, decreasing with increasing flight distances.



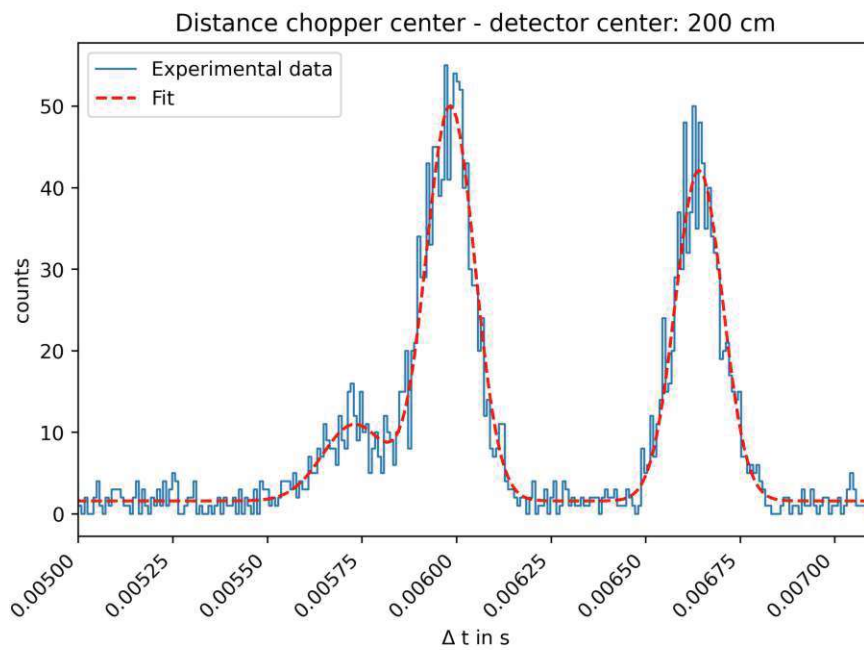
(a) Measurement data and fit for 10 cm between chopper and detector. Resulting maxima at  $t_1 = 5.389 \cdot 10^{-3} \pm 3.29 \cdot 10^{-6}$  s. Measurement duration: 10 min



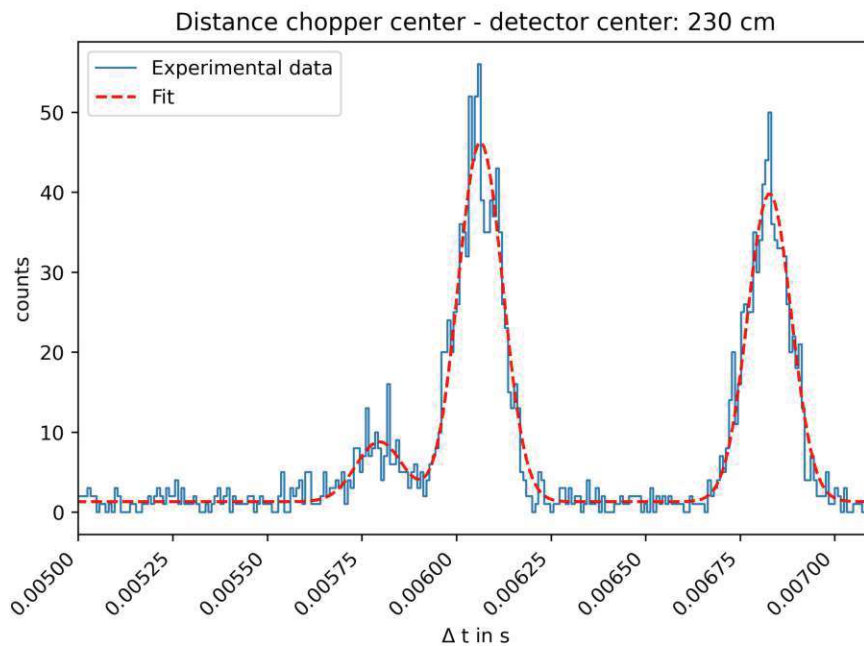
(b) Measurement data and fit for 100 cm between chopper and detector. Resulting maxima at  $t_1 = 5.634 \cdot 10^{-3} \pm 8.28 \cdot 10^{-6}$  s and  $t_2 = 5.975 \cdot 10^{-3} \pm 9.47 \cdot 10^{-6}$  s. Measurement duration: 10 min



- (c) Measurement data and fit for 150 cm between chopper and detector. Resulting maxima at  $t_1 = 5.804 \cdot 10^{-3} \pm 2.13 \cdot 10^{-5}$  s,  $t_2 = 6.303 \cdot 10^{-3} \pm 2.83 \cdot 10^{-5}$  s and  $t_3 = 5.61 \cdot 10^{-3} \pm 3.77 \cdot 10^{-5}$  s. Measurement duration: 15 min



- (d) Measurement data and fit for 200 cm between chopper and detector. Resulting maxima at  $t_1 = 5.986 \cdot 10^{-3}$  s,  $t_2 = 6.643 \cdot 10^{-3}$  s and  $t_3 = 5.743 \cdot 10^{-3}$  s. Measurement duration: 20 min



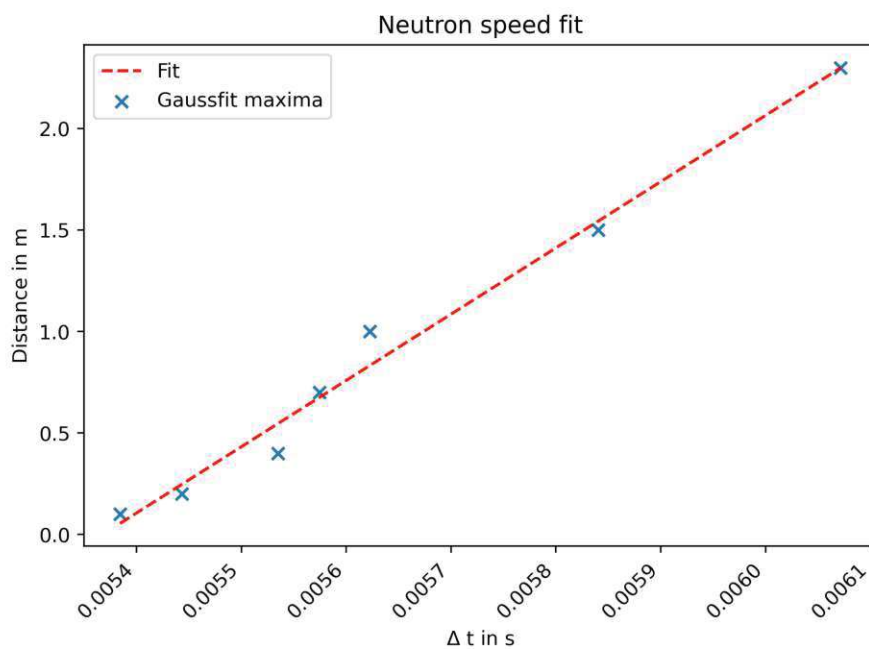
(e) Measurement data and fit for 230 cm between chopper and detector. Resulting maxima at  $t_1 = 6.067 \cdot 10^{-3} \pm 3.41 \cdot 10^{-6}$  s,  $t_2 = 6.830 \cdot 10^{-3} \pm 5.24 \cdot 10^{-6}$  s and  $t_3 = 5.803 \cdot 10^{-3} \pm 1.06 \cdot 10^{-5}$  s. Measurement duration: 20 min

**Figure 4.2:** Collected measurement data from the n-TOF measurements performed with the Canberra 20NH20/1TP  $^3\text{He}$  detector.

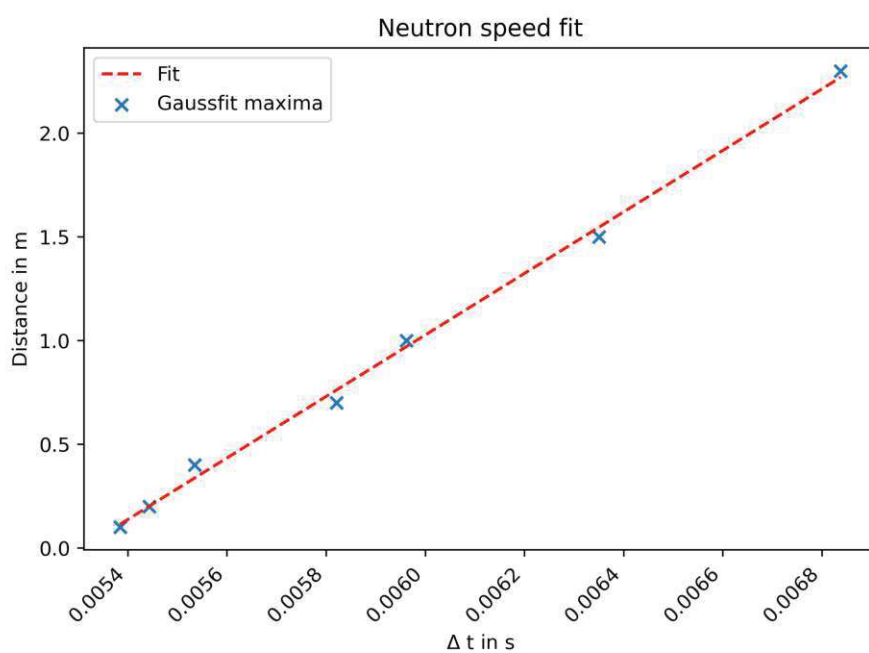
In order to evaluate the gathered data for each peak and set of measurements, each maximum position was taken with its corresponding distance between chopper and detector. This set of (time, distance) points was then used to create a linear fit with distance as function of time (Figure 4.3). The slope determines the velocity corresponding to each peak. Effectively, the slope yields the neutron speed used in Equation (2.2), the results are displayed in Table 4.4.

Peak	Speed [m/s]	Wavelength [ $\text{\AA}$ ]
1, VacuTec	3266	1.211
1, Canberra	3155	1.254
2, VacuTec	1483	2.668
2, Canberra	1516	2.610
3, VacuTec	5579	0.709
3, Canberra	4236	0.934

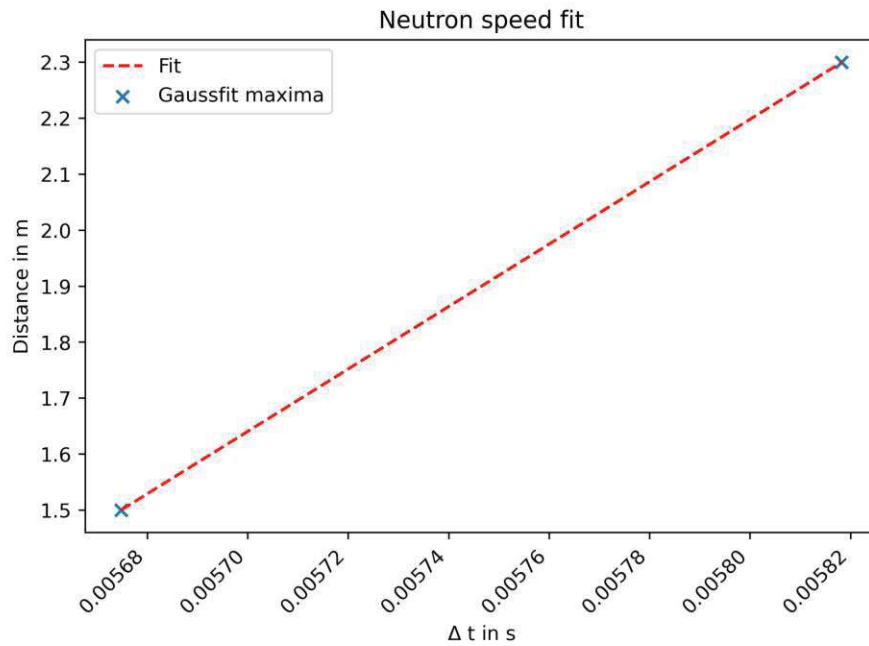
**Table 4.4:** Collected neutron speeds and wavelengths.



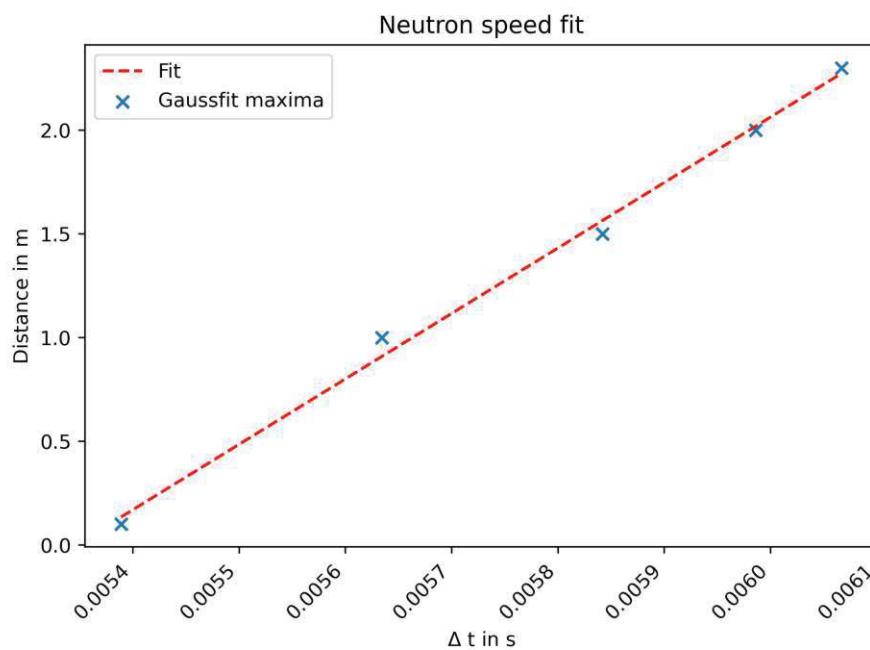
(a) Linear fit for peak 1 using the dataset of the measurements with the VacuTec Type 70 063 detector. The resulting neutron speed is 3266 m/s.



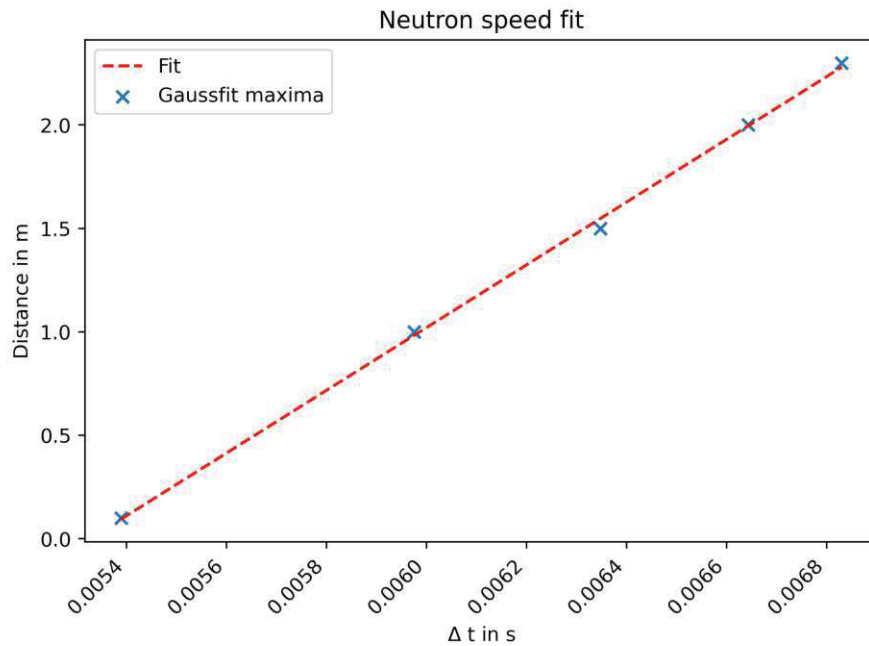
(b) Linear fit for peak 2 using the dataset of the measurements with the VacuTec Type 70 063 detector. The resulting neutron speed is 1483 m/s.



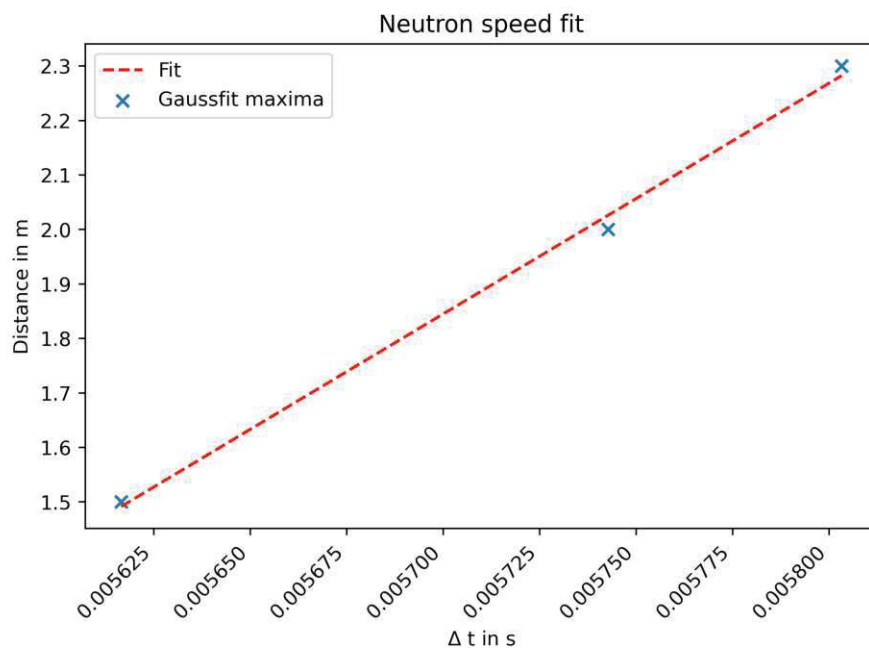
- (c) Linear fit for peak 3 using the dataset of the measurements with the VacuTec Type 70 063 detector. The resulting neutron speed is 5579 m/s.



- (d) Linear fit for peak 1 using the dataset of the measurements with the Canberra 20NH20/1TP detector. The resulting neutron speed is 3155 m/s.



(e) Linear fit for peak 2 using the dataset of the measurements with the Canberra 20NH20/1TP detector. The resulting neutron speed is 1516 m/s.



(f) Linear fit for peak 3 using the dataset of the measurements with the Canberra 20NH20/1TP detector. The resulting neutron speed is 4236 m/s.

**Figure 4.3:** Linear fits for determining the speeds of present neutrons using all gathered datasets.

The fit functions used to create Figure 4.1 and 4.2 were then used to determine the beam compositions. The area under a peak represents the amount of neutrons contributing to it; the total amount of neutrons detected is the sum of the peak areas. The percentage of neutrons with a certain speed can be determined as the number of neutrons under that peak divided by the total number of neutrons. This can be done at each distance individually. However, due to the fact that the third peak arises only at higher distances between detector and chopper, the calculations were performed for the measurements at a distance of 230 cm. The calculated beam compositions are shown in Table 4.5, the corresponding wavelengths of peak 1 and peak 2 have been averaged. For peak 3, only the result from the Canberra 20NH20/1TP was considered because peak 3 was clearly visible in Figure 4.1d but only found by the algorithm in Figure 4.1c.

Detector	Peak 1 (1.233 Å)	Peak 2 (2.639 Å)	Peak 3 (0.822 Å)
VacuTec 70 063	49.54%	40.55%	9.91%
Canberra 20NH20/1TP	52.08%	42.56%	5.36%

**Table 4.5:** Composition of the neutron beam, measured with two different neutron detectors without accounting for the different detection efficiencies at each wavelength.

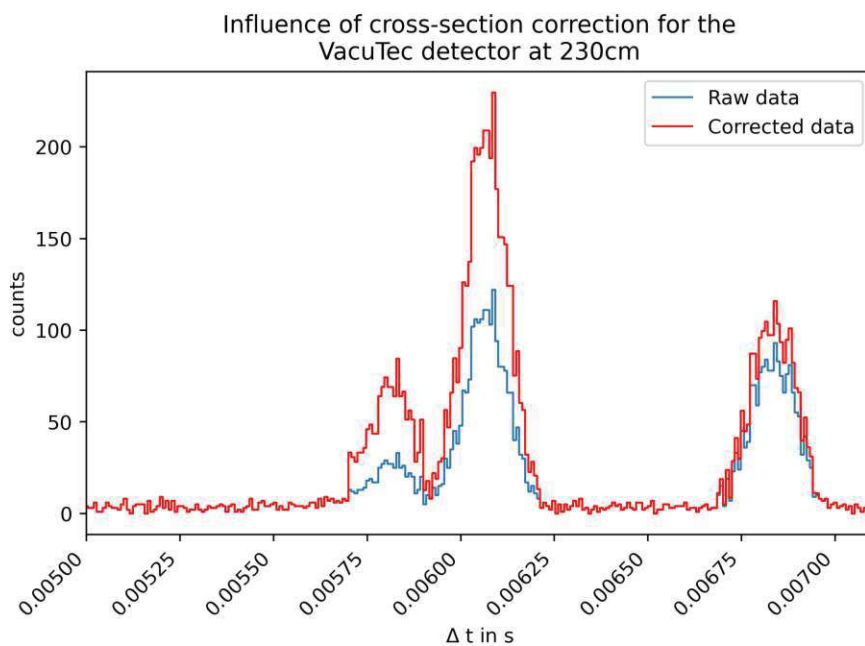
Table 4.5 assumes, that the detection efficiency for all measured neutrons is the same, taking the first approximated efficiency values from subsection 3.2. Corrections of this assumption can be made using the data of Table 4.8, which gives numerically computed values for the detector efficiencies at the relevant speeds. Weighting the peak areas with the corresponding efficiencies finally yields the actual beam composition, shown in Table 4.6 and Figure 4.4. The same calculation was repeated by manual evaluation of the data and calculating peak areas and errors, resulting in Table 4.7.

Detector	Peak 1 (1.233 Å)	Peak 2 (2.639 Å)	Peak 3 (0.822 Å)
VacuTec 70 063	55.14%	29.86%	15.00%
Canberra 20NH20/1TP	59.49%	32.18%	8.33%
Averages	57.32%	31.02%	11.66%

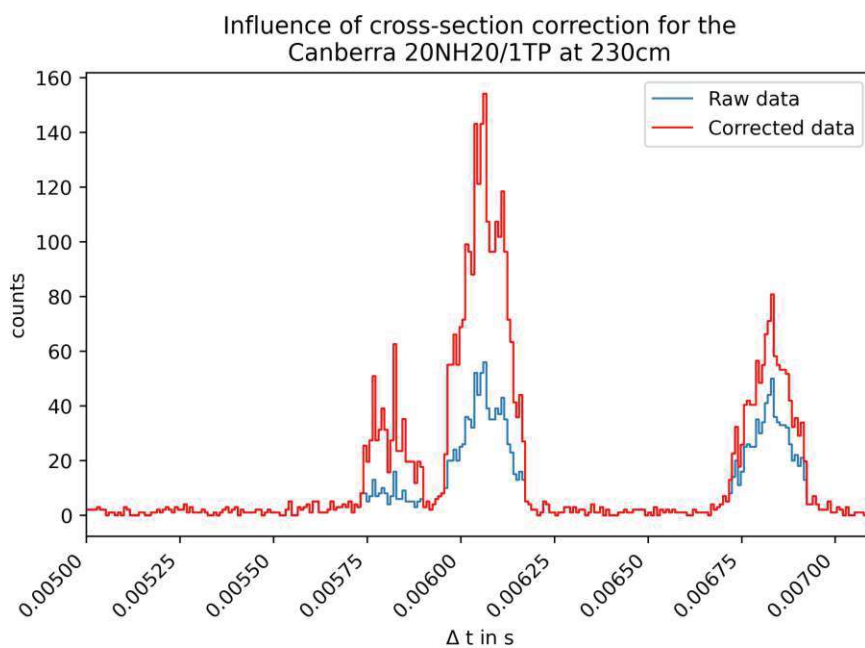
**Table 4.6:** Efficiency corrected composition of the neutron beam, measured with two different neutron detectors.

Detector	Peak 1 (1.233 Å)	Peak 2 (2.639 Å)	Peak 3 (0.822 Å)
VacuTec 70 063	53.22 ± 1.93%	28.46 ± 1.08%	18.31 ± 1.01%
Canberra 20NH20/1TP	58.74 ± 2.15%	29.02 ± 1.16%	12.24 ± 7.61%
Averages	55.98 ± 0.81%	28.75 ± 0.23%	15.28 ± 0.70%

**Table 4.7:** Manually calculated efficiency corrected composition of the neutron beam, measured with two different neutron detectors.



(a) Efficiency correction for the VacuTec 70 063.



(b) Efficiency correction for the Canberra 20NH20/1TP.

**Figure 4.4:** Comparison of the raw measurement data vs the measurement data with efficiency correction for each peak.

### 4.3 Detector efficiency of various gas filled proportional counters

The previously determined neutron speeds now allow to calculate (using equation (2.17)) the thermal neutron absorption cross-sections needed, for both  $^3\text{He}$  and  $^{10}\text{B}$ . The reference points are the known cross-sections for 25 meV, which correspond to a neutron speed of 2200 m/s.

Detector	2200 m/s	3210.5 m/s	1499.5 m/s	4907.5 m/s
VacuTec Type 70 063	66.906%	53.124%	80.255%	39.078%
Canberra 20NH20/1TP	48.254%	36.327%	61.961%	25.566%
Canberra 0.5NH1/1KF	62.670%	49.102%	76.425%	35.714%
BF <sub>3</sub> -counter	29.879%	21.589%	40.590%	14.710%

**Table 4.8:** Relative detector efficiencies at the different occurring neutron speeds. 2200 m/s was kept as a reference.

Using the average beam composition determined in Table 4.7 and the calculated efficiencies at each neutron speed from Table 4.8, the theoretical expectation for detector efficiency in our system can be calculated as the sum of the three efficiencies corresponding to the speeds, each one weighted with its average fraction of the beam. The resulting expected efficiencies are shown in Table 4.9. The displayed error is a direct result from the uncertainty in determining the beam composition.

Detector	Reference efficiency (2200 m/s)	Expected efficiency
VacuTec Type 70 063	66.906%	58.78 ± 0.54%
Canberra 20NH20/1TP	48.254%	42.06 ± 0.37%
Canberra 0.5NH1/1KF	62.670%	54.91 ± 0.50%
BF <sub>3</sub> -counter	29.879%	26.00 ± 0.22%

**Table 4.9:** Detector efficiencies estimated for thermal neutrons and calculated for the average beam composition as of Table 4.7.

In order to find out how accurate those calculations are, the obtained results will be compared with physical measurements. The absolute present neutron flux is taken as an average of the (cross-section corrected) measurements for the 416 keV, 1097 keV and 1293 keV gamma lines. Results from the 1507 keV and 2112 keV line were discarded due to their large error margins. Without accounting for cross-section correction of the neutron activation analysis, we obtain an average flux of  $2250 \pm 240 \text{ cm}^{-2}\text{s}^{-1}$ . The absolute cross-section corrected averaged neutron flux then is  $2580 \pm 275 \text{ cm}^{-2}\text{s}^{-1}$ . This value can now be compared to the neutron flux measured by the gas-filled proportional counters in order to empirically determine their efficiency. The results of this comparison are shown in Table 4.10. The errors of the average flux for each detector are calculated as the square root of the measured flux, as those measurements follow a poisson distribution. The

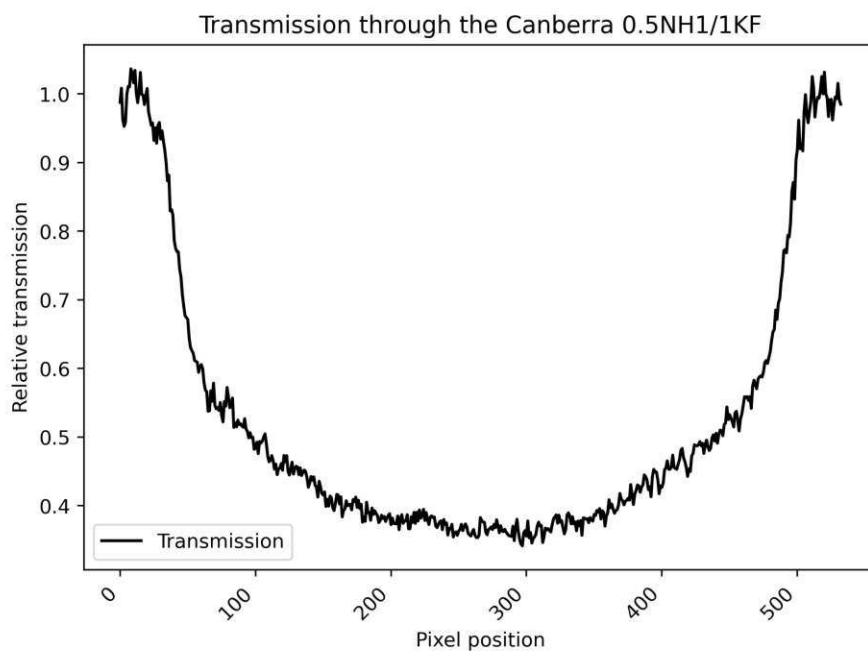
error in empirical efficiency is influenced by the error of the average flux and the error of the absolute neutron flux present. It was obtained using propagation of uncertainty. The expected efficiencies were calculated using Equations (2.13) and (2.14), ignoring the influence of beam divergence. This choice was made for two reasons: firstly, the beam divergence has not been determined yet. Any calculation using it would be made with dummy values. Secondly, quick calculations assuming  $1^\circ$  and  $10^\circ$  beam divergence show that its influence is negligible due to the small detector sizes. Even for the largest detector type used, the Reuter-Stokes BF<sub>3</sub>-counter, the diversion in expected efficiency is only about one percentage point.

Detector	Average flux [ $\text{m}^{-2}\text{s}^{-1}$ ]	Empirical efficiency [%]
VacuTec Type 70 063 00022	$1600 \pm 40$	$62 \pm 7$
VacuTec Type 70 063 00023	$1560 \pm 40$	$61 \pm 7$
VacuTec Type 70 063 00025	$1550 \pm 40$	$60 \pm 7$
Canberra 20NH20/1TP B0100	$1390 \pm 40$	$54 \pm 6$
Canberra 20NH20/1TP B0101	$1280 \pm 40$	$50 \pm 5$
Canberra 0.5NH1/1KF	$1410 \pm 40$	$55 \pm 6$
Reuter-Stokes BF <sub>3</sub> -counter	$1120 \pm 30$	$43 \pm 5$

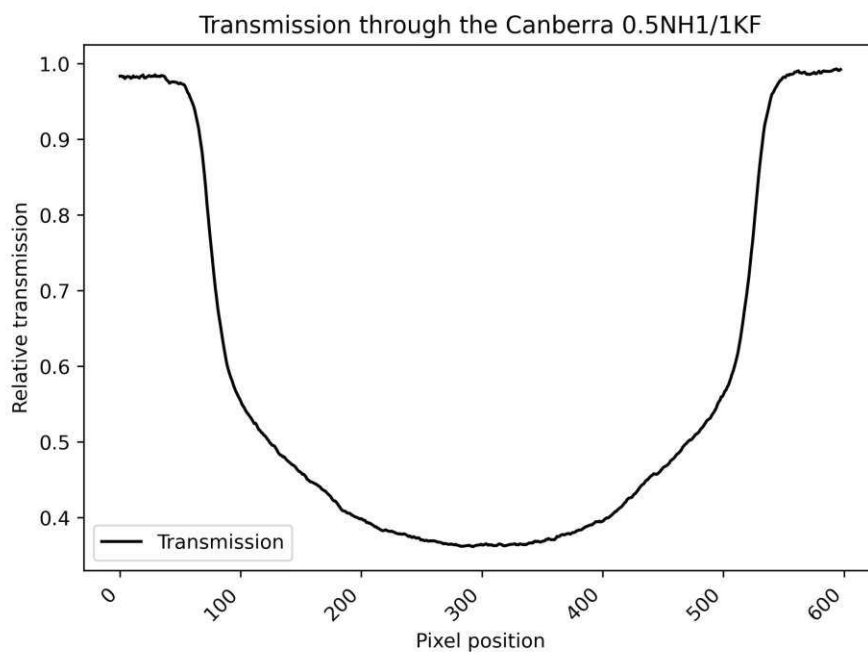
**Table 4.10:** Empirical efficiencies of all used detectors. The added numbers in the detector names for VacuTec Type 70 063 and Canberra 20NH20/1TP signify the internal numbering of the detectors at Atominstitut.

#### 4.4 Evaluation of the neutron radiography image

Figure 3.8 gives the opportunity to investigate the detector efficiency of the Canberra 0.5NH1/1KF detector in a white neutron beam. In neutron radiography, the image is recorded by measuring the neutrons transmitted through the sample. When additionally recording the background- and noise with closed shutter, the image can be further processed to account for those disturbances. This processed image can be interpreted in a similar fashion as a measurement with the detector. To determine the transmission, an image of the white beam without sample is recorded. The relative transmission can be obtained by dividing the neutron counts of those two images pixel by pixel and normalizing it to grey values between 0 and 1. Each pixel then contains the transmission at a certain point, displayed by the corresponding grey value. Black pixels display no transmission while white pixels represent 100% transmission. Those grey values can also be read out and plotted as a function of position. It is possible to either plot the grey values of a single line of pixels or to average over multiple lines. The results can be seen in Figure 4.5. Averaging over the entire detector width yields an average transmission of 48.23%, corresponding to an absorption or efficiency of 51.77%.



(a) Transmission along a single line of pixels perpendicular to the cylinder axis.



(b) Averaged transmission along a line of pixels.

**Figure 4.5:** Relative transmission through the active region of the Canberra 0.5NH1/1KF detector.

## 5 Discussion

### 5.1 Neutron activation analysis

Forming the basis to the empirical determination of detector efficiencies, the resulting actual flux present is a key parameter and knowing it as good as possible was the goal of this experiment. The choice of Indium as a probe material provided the option for an internal consistency check of the measurements due to the 5 major characteristic gamma lines. Additionally, measurements were performed with two different probes and evaluation was performed using three different methods. This way, a total of 6 datasets (2 probes times 3 evaluation methods) were obtained. Each set was individually checked by comparing the calculated flux from the different lines and the sets were compared among each other. As expected, the resulting fluxes from the 416 keV, 1097 keV and 1293 keV lines were found to be in reasonably good agreement over the performed measurements. What proved to be difficult was adding the 1507 keV line and the 2112 keV line into consideration. Because they have the lowest probability to occur at an  $^{115}\text{In}$ -decay and the efficiency of the gamma detector decreases with increasing incident photon energy, low count rates were expected for those lines. The approximation performed in sub-subsection 3.1.2 proved to be quite accurate in predicting the order of magnitude for the expected counts. With as little as 5–34 cts for the higher energy gamma lines simply could not reliably be taken into consideration because their margin of error is way too large. While the average margin of error was around 10% for most measurements, it reached up to 56% for those lines according to Table 4.3. Analysis using InterSpec proved no more reliable for those high energy gamma lines, yielding results with unreasonably low uncertainties. As the measurement data follow a Poisson distribution, the standard deviation is calculated as  $\sqrt{n}$  with  $n$  being the total counts associated with a gamma line. However, human error adds an additional disadvantageous influence factor, as the peaks for the gamma lines in question had to be added manually, which was quite challenging. With rarely more than 3 counts per channel, the 1507 keV peak and the 2112 keV peak were basically indistinguishable from the background spectrum. The on-site evaluation software also was unable to locate said two peaks. Due to the overwhelming number of reasons, they were finally not taken into account for evaluation. For the 416 keV, 1097 keV and 1293 keV lines, the error margins of both manual evaluation and InterSpec evaluation are in good agreement (6.95%–10.01%); the on-site software calculated larger error margins. This can be attributed to the fact, that it treated most of the found peaks as multiplets, resulting in the larger error margins.

Due to the three different wavelengths present, the results displayed in Tables 4.1–4.3 need to be multiplied by a factor of  $1.144 \pm 0.009$ . This correction by about 15% is quite small and provides an argument for simply using the assumption of a monochromatic beam with 25 meV in applications where precision is not of importance.

There are a few key factors influencing the obtainable precision of the neutron activation analysis results as the calculated flux is directly dependant of the gamma counts,

which can be influenced in a few ways. Firstly, longer irradiation of the probes could to a certain degree increase the number of gammas counted by directly increasing the induced activity. However, when irradiating a sample activity reaches saturation after sufficiently long exposure to the neutron beam, meaning that the number of nuclei decaying per time unit is the same as the number of activated nuclei per time unit. Hence longer exposure offers only very limited capabilities to improve the measurements. A second possibility would be to perform the measurement with the gamma detector over a longer time interval. To a certain degree this method provides more counts because more decays occur during readout. Nuclear decay follows an exponential decay law. Consequentially, doubling the readout time does not double the total gamma counts. Additionally, while the signal originating from the activated probes weakens over time, the background from natural radioactivity stays the same. Hence increasing the measurement duration also decreases the signal:noise ratio. Finally, a simple method to increase the number of obtained gammas would be to increase the size of the irradiated surface by increasing the size of the aperture. While this should linearly increase the produced activity, it was decided to keep the small  $5\text{ mm} \times 5\text{ mm}$  aperture for maximum comparability of the results from neutron activation analysis and proportional counter measurements. Furthermore, the maximum increase in irradiated area would be to a surface area of  $\pi\text{ cm}^2$ , resulting in about 12.57 times more irradiated area. The resulting improvement in uncertainty was not seen as sufficiently significant to distort the comparability between neutron activation analysis and proportional counter measurements.

The obtained average neutron flux of  $2580 \pm 275\text{ cm}^{-2}\text{s}^{-1}$  reasonably fits the expectations formed by prior results. However, one could make an argument that this result is still too low as the calculated fluxes for the 1293 keV line contain several outliers on the lower end.

## 5.2 Spectral analysis of the neutron beam

Determining the spectrum of the neutrons present at the tangential beam tube at the tangential beam tube was crucial for the ability to accurately perform calculations about detector efficiencies and evaluations of the neutron activation analysis because all those calculation depend on the neutron absorption cross section, which is energy dependant.

Being able to identify three different neutron energies was surprising as prior measurements could only resolve two. However, it can not be said with certainty that the three found neutron energies are all that are present in the beam. Extending the distance between chopper and detector even further might yield even more different energies. When looking at Figures 4.1 and 4.2 and comparing the peak areas to each other, one can observe that the ratio of the peak areas of peak 1 and peak 2 stays very similar over all distances. From that one can make the assumption, that the third peak should also follow this behaviour and stay relatively small. Furthermore, if a fourth peak were to occur at larger distance, it is plausible to assume that its relative fraction of the beam would be

even smaller than the fraction of peak 3. The resulting hypothetical amount of neutrons from energy 4 would only make up a few percent of the total beam and due to their energy being even higher (and absorption cross-section even lower) than this of peak 3, their detection probability would be very low. Hence it is reasonable to neglect a hypothetical fourth neutron energy because it would barely influence any measurements taken.

Overall the measurements with both the Canberra 20NH20/1TP and the VacuTec Type 70 063 were found to be in good agreement with each other. For determining the speed of the fastest neutrons with the VacuTec detector, the fit for the measurement at 150 cm distance was done with the fit function for triple peaks despite displaying only two dominant peaks. However, a rising structure can be perceived at the left flank of peak 1. The present wavelengths were determined to be 1.233 Å, 2.639 Å and 0.822 Å. They roughly follow Bragg's law as can be seen in Figure 5.1.

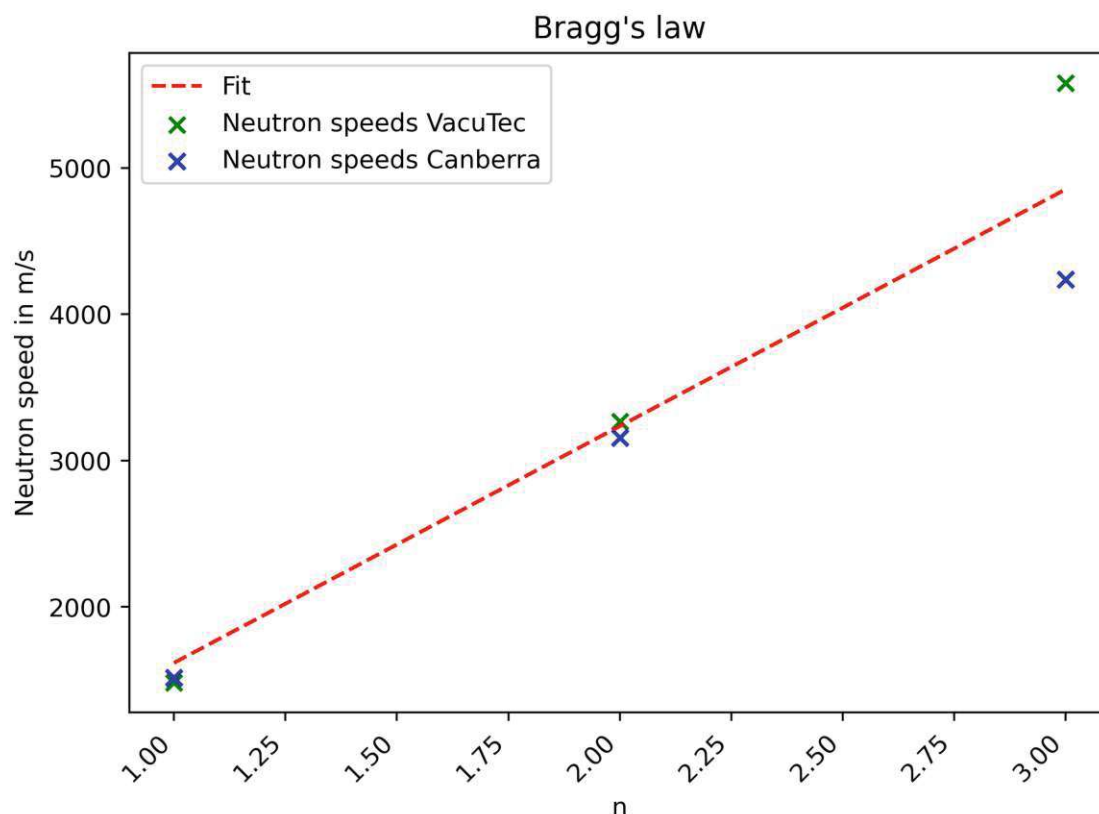


**Figure 5.1:** Linear fit to show the agreement between the obtained neutron speeds and Bragg's law.

The determined spectral composition of the beam displayed in Table 4.6 show excellent agreement for both used detectors when measuring the slowest neutrons. With increasing

neutron speeds, the relative deviation increases but the general behaviour is similar for both systems. The reason for this is that the VacuTec Type 70 063 simply has significantly better detection probabilities over all observed energies compared to the Canberra 20NH20/1TP. The five times higher particle density in the squashed detector can not compensate for the significantly larger mean path length through the cylindrical VacuTec counter. The expected advantage of the used Canberra detector was a reduced peak width due to the narrowly defined position uncertainty in detection. However, this behaviour could not be observed. This suggests, that under the circumstances of the measurement the impact of the small position uncertainty in detection for the Canberra 20NH20/1TP is smaller than other effects such as the size of the chopper window, which seems to dominate peak width in the performed measurements.

Determining the composition of the neutron beam is only possible as soon as the detector efficiencies for the different wavelengths present are known. Peak areas can be obtained either via integration over each peak in the fit or by comparing the total counts from the measurement in each peak. Both methods yield similar results. Dividing the peak areas by the detector efficiencies gives the actual peak areas. Dividing the area of one peak by the sum of all peak areas finally gives the fractions of each wavelength.

### 5.3 Detector efficiency of various gas filled proportional counters

With the precise information about the present neutron wavelengths, it was possible to estimate the detector efficiencies for the specific neutron beam used. Comparing the calculation results in Table 4.9 to the measurement results of Table 4.10 one can see how good the analytical formula for calculating the detector efficiencies fits the reality. For the cylindrical  $^3\text{He}$ -counters, the calculation results for detector efficiency considering the present energy spectrum lies mostly within the error margin of the empirical data. For the squashed  $^3\text{He}$ -counter, despite the supposedly way simpler calculation, the expected efficiency settles between two and three error margins away from the empirical results. The values for the Reuter-Stokes  $\text{BF}_3$  detector are so far apart from each other, that the formula seemingly can not accurately predict the efficiency of this proportional counter. However a possible reason for the strong deviation in this case may also be that basically no technical data were available for this detector and almost all parameters had to be approximated. A definite trend seen in comparison between theoretical estimate and empirical result is that the formula consistently underestimates the detector efficiency when considering multiple wavelengths.

The first calculations were made assuming a monochromatic thermal (2200 m/s) neutron beam. The results of this first estimate surprisingly match the experimental data significantly better than the more complicated calculation which considered multiple wavelengths: The efficiency assuming monochromatic thermal neutrons almost perfectly match the experiment for the VacuTec Type 70 063 and the Canberra 0.5NH1/1KF and even for the Canberra 20NH20/1TP the deviation is significantly lower. If all the present neutron

wavelength would represent the same fraction of the beam, the average wavelength would almost coincide with the wavelength of thermal neutrons. However, this is not the case as the measurements in subsection 4.2 clearly prove. A more likely reason for the found discrepancy lies in the absolute neutron flux taken into account for the empirical results. When excluding the obtained flux values from the 1293 keV line, the calculate average neutron flux present increases by about  $200 \text{ cm}^{-2}\text{s}^{-1}$  and the results in Table 4.10 approach the expected values very well. However, for most used detectors, the expected efficiency lies within the error margin of the empirical efficiency. The exception of this is the  $\text{BF}_3$  detector, its results do not seem to have any correlation with the analytical formula at all. Due to the fact that basically no technical data was available for it, this does not come as a surprise as well.

Comparing the results of three VacuTec Type 70 063 to each other shows that they are almost perfectly comparable among each other, meaning they can be used interchangeably without biasing measurement results. When comparing the two used Canberra 20NH20/1TP detectors, slightly larger deviations were noted. A possible explanation for this deviation could be minor differences in their internal  $^3\text{He}$ -pressure. However, both results for this detector type lie within each others error margin, suggesting that data obtained by those are comparable.

For further usage of the examined detectors, especially the VacuTec Type 70 063 and the Canberra 0.5NH1/1KF, a table of their efficiencies depending on the used apertures has been created and can be seen below in Table 5.1. Those calculations were not performed for the Canberra 20NH20/1TP because its cuboid active volume renders them obsolete. The Reuter-Stokes counter has been excluded from the table as well because the analytical formula failed describing its behaviour by a large margin.

Aperture size [mm])	VacuTec Type 70 063 [%]	Canberra 0.5NH1/1KF[%]
$w = 1$	$59.08 \pm 0.55$	$56.45 \pm 0.52$
$w = 5$	$58.78 \pm 0.54$	$54.91 \pm 0.50$
$w = 10$	$57.75 \pm 0.53$	$47.46 \pm 0.43$
$w = 15$	$55.74 \pm 0.51$	$47.42 \pm 3.78$
$w = 20$	$51.71 \pm 0.47$	$47.42 \pm 3.78$
$w > 20$	$49.87 \pm 0.45$	$47.42 \pm 3.78$
$r = 2.5$	$58.86 \pm 0.54$	$55.32 \pm 0.51$
$r = 5$	$58.59 \pm 0.54$	$50.47 \pm 0.46$
$r = 7.5$	$56.66 \pm 0.52$	-
$r = 10$	$54.00 \pm 0.49$	-

**Table 5.1:** Predicted efficiencies of the cylindrical  $^3\text{He}$  detectors for common aperture sizes. Width  $w$  for rectangular/quadratic and radius  $r$  for circular apertures.

For rectangular apertures, the efficiency stays constant as soon as the width of the aperture exceeds the radius of the detector. Circular apertures with aperture radii greater than

the detector radius are not commonly used, therefore no calculations were performed for this scenario. It can be clearly observed, that smaller apertures directly result in higher detection efficiencies. The discrepancy in efficiency between tiny spot or slit apertures positioned in front of the detector center and apertures larger than the detector widths (which equal a detector without aperture) is about 19 percentage points for the VacuTec 70 063 but only about 9 percentage points for the Canberra 0.5NH1/1KF. This shows that larger cylindrical detectors suffer from a larger loss of efficiency when the aperture size approaches their radius. For smaller apertures, the longer average path length makes detectors with larger radii the more efficient choice.

As already mentioned in subsection 4.3, while beam divergence definitely has an effect on the detector efficiency, it was found that it is negligible compared to other influence factors such as aperture geometry. The average effect of beam divergence is an increase in path length through the detector medium. Due to the detector sizes, the resulting potential increases in path length and furthermore detector efficiency can be neglected. The only case where assumed beam divergences made a somewhat significant difference was the largest detector, the Reuter-Stokes  $\text{BF}_3$ -counter. Even there, the impact of divergence correction results in an efficiency increase of only two percentage points. Considering the effects of beam divergence was still not enough to push the calculated efficiency even close to the obtained experimental results. Consequentially, this detector should be further examined at varying operating voltages to find its actual working point. If this does not suffice, the assumed technical parameters of this detector are simply too far off its actual specifications to make accurate predictions.

The 51.77% efficiency of the Canberra 0.5NH1/1KF obtained by analyzing the neutron radiography image is of similar order of magnitude as the calculations in Table 5.1 for apertures with large widths. This underlines that  $^3\text{He}$  counters are mostly sensitive to neutrons with lower energies such as thermal neutrons. The fast component of the white neutron beam mostly contributes to transmission through the detector as the neutron absorption cross-section decreases with increasing neutron energy.

## 6 Conclusion

While the manufacturers of neutron detectors usually give a nominal sensitivity of their products, it can be of use to re-evaluate the detector efficiency in the setting where the detector is used. Given sensitivity usually assumes that the whole detector cross-section is exposed to the neutron flux, therefore neglecting the influence of apertures or the spectral distribution of the measured neutrons. When calculating the expected detector efficiency without apertures for neutrons with a speed of 2200 m/s, the results are in good agreement with the given values from the manufacturers.

Neutron activation analysis proved to be a viable method to determine the present neutron flux. The obtained flux has an error of about 11%, which is sufficient for the comparisons made. This could still be improved by increasing the apertures area. Increasing the aperture size by a factor of 4 should cut the obtained error in half. Performing the gamma measurement over longer times could also yield some improvement, to a certain degree. Evaluation is fairly simple, as is accounting for different neutron wavelengths via their different cross-sections. The software InterSpec proved to be reliable in evaluation of the gamma spectra and provides numerous useful tools helping with the evaluation. Choosing Indium over gold as probe material helped not only with allowing multiple channels to calculate the neutron flux but also by drastically reducing the required times for irradiation and readout due to its shorter half-life.

Neutron time-of-flight measurements proved to be a reliable tool to determine the energy spectrum and furthermore the composition of the neutron beam. Three different wavelengths and their contribution to the beam could be identified with reasonable precision. While it is possible that neutrons with even higher energies are a part of the beam, the fraction those would make up should be well below 5%. To resolve higher neutron energies, the distance between chopper and detector would need to be increased. This would be possible up to a certain point but there is an absolute limit due to the finite size of the reactor hall.

When comparing the performed measurements with the VacuTec Type 70 063 and the Canberra 20NH20/1TP, results generally are in good agreement. Due to the lower efficiency of the Canberra detector, its results show larger relative margins of error. While being specifically designed for time-of-flight spectroscopy, no such advantages could be observed in this experiment. The widths of the peaks were near identical with both the VacuTec and the Canberra detector. The reason for this may be that the detector width was negligible compared to the total travelled distance in both cases.

When investigating the resemblance of the obtained wavelengths with Bragg's law (Equation (2.1)), the agreement between measurements and theory is not perfect. One reason for the diversion is that the wavelength of peak 3 was determined using only one detector. With a second data point to compensate the diversion, better agreement may be achieved.

For determining the beam composition from peak areas, both comparing the areas of the peaks in the fit functions and manually calculating the peak areas from the total counts are valid options and yield quite similar results. The majority of the beam are 1.233 Å neutrons ( $\sim 56\%$ ), the remaining neutrons are mostly at 2.639 Å ( $\sim 30\%$ ). Only a small fraction ( $\sim 14\%$ ) of the beam consists of the faster 0.822 Å neutrons.

Calculating the detector efficiencies for all used counters by comparing the obtained neutron flux from neutron activation analysis to the counted neutrons of each detector showed some unexpected results. While the most empirical results were in fairly good agreement with the analytical formula, the Canberra 20NH20/1TP B0100 showed a larger deviation from the expectation than the other evaluated detectors. The empirical efficiency of the investigated  $\text{BF}_3$  detector lies far above the calculated expectation. A possible reason may be a too high operating voltage, causing secondary ionisation in the filling gas and therefore distorting the neutron induced signal. However, precise results could not be expected from a device where no operating parameters are known. Researching the working point of this detector or its actual specifications may be of interest for its future use.

In addition, for the cylindrical  $^3\text{He}$ -detectors the empirical efficiency is quite close to their efficiency when assuming a monochromatic thermal neutron beam. This suggests, that assuming the investigated neutron beam as monochromatic and thermal is a valid assumption for applications where knowing the spectral composition of the beam is not required.

While the measurement results arguably still are not the best, with error margins in the 10%-regime, the information gained is still sufficiently precise to use it for the CRAB experiment in the future. The desired neutron flux of about  $270\text{ cm}^{-2}\text{ s}^{-1}$ , which will be achieved using neutron beam optics, can be measured sufficiently precise using the information of table 5.1.

This thesis provides a set of tools which can generally help to simplify measurements of the beam distribution in the future. Table 5.1 provides estimates for detector efficiencies in different combinations of counters and apertures. Table 4.10 gives a good comparison between the different detectors, showing that especially those of the same types may be used interchangeably. This information can be used especially to save time in the future while at the same time gaining results that are better understood now.

## List of Figures

2.1	Decay scheme of $^{116}\text{In}$ [9]. The red arrows signify the characteristic gamma energies used to calculate the neutron flux. The blue and black arrows show minor nuclear transitions; their probabilities to occur are too small to give statistically relevant results. Transition energies are given in keV. . . . .	9
2.2	Neutron absorption cross-section $\sigma_a$ for $^3\text{He}$ , $^{10}\text{B}$ and $^6\text{Li}$ as a function of incident neutron Energy [17]. . . . .	11
2.3	Example pulse height spectrum of one of the used $^3\text{He}$ -counters . . . . .	13
2.4	Sketch for calculation of the path length of neutrons through a cylindrical detector. The neutron beam comes from the right. The black rectangles portray an aperture. . . . .	14
2.5	Sketch for deriving the correction factor necessary to account for divergence. The neutron beam comes from the right. The black rectangle portrays an aperture. . . . .	15
3.1	Chopper used for neutron time-of-flight measurements. . . . .	17
3.2	Mount for the Indium probes. . . . .	20
3.3	Construction design of the detector mount. Designed by Roman Gergen. Fabrication: Atominstitut Workshop. . . . .	22
3.4	Borated polyethylene detector holder without inserted detector. . . . .	23
3.5	The VacuTec 70 063 $^3\text{He}$ detector . . . . .	24
3.6	The Canberra 20NH20/1TP $^3\text{He}$ detector. . . . .	26
3.7	The Canberra 0.5NH1/1KF $^3\text{He}$ detector. . . . .	27
3.8	Neutron radiography image of the Canberra 0.5NH1/1KF $^3\text{He}$ detector. . . . .	29
3.9	Reuter Stokes $\text{BF}_3$ counter with detector mount on the left. . . . .	29
3.10	Loading spectra in InterSpec. . . . .	31
3.11	Setting up reference lines. In this case, $\text{In}116\text{m}$ was used. . . . .	32
3.12	Manual addition of a peak at 1507 keV. Due to the low intensity, it is barely discernable from the background. . . . .	32
3.13	Results screen of the peak search algorithm. Peaks at the energies of a reference line are displayed in a chosen colour. . . . .	33
3.14	Complete obtained spectrum with peak characteristics needed for further evaluation. Foreground 1 (white) and foreground 2 (red) originate from two different measurements, the background is displayed in blue. Reference lines and the corresponding peaks in the spectrum are shown in green. . . . .	34
4.1	Collected measurement data from the n-TOF measurements performed with the VacuTec Type 70 063 $^3\text{He}$ detector. . . . .	39
4.2	Collected measurement data from the n-TOF measurements performed with the Canberra 20NH20/1TP $^3\text{He}$ detector. . . . .	42
4.3	Linear fits for determining the speeds of present neutrons using all gathered datasets. . . . .	45
4.4	Comparison of the raw measurement data vs the measurement data with efficiency correction for each peak. . . . .	47

---

4.5	Relative transmission through the active region of the Canberra 0.5NH1/1KF detector. . . . .	50
5.1	Linear fit to show the agreement between the obtained neutron speeds and Bragg's law. . . . .	53

## List of Tables

2.1	Energies of characteristic gammas and probabilities that they occur in a decay of $^{116}\text{In}$ [9]. . . . .	10
3.1	Probabilities for detecting characteristic gamma caused by a neutron. Detection probability is the product of absorption probability, natural abundance of $^{115}\text{In}$ , line probability and detector efficiency. . . . .	19
3.2	Operating parameters of the VacuTec 70 063 $^3\text{He}$ detector. Nominal operating voltage, $^3\text{He}$ -pressure, active volume and Manufacturer sensitivity were taken or calculated from [20]. . . . .	25
3.3	Operating parameters of the Canberra 20NH20/1TP $^3\text{He}$ detector. Nominal operating voltage, $^3\text{He}$ -pressure, active length and section were taken or calculated from [21] . . . . .	26
3.4	Operating parameters of the Canberra 0.5NH1/1KF $^3\text{He}$ detector. Nominal operating voltage, $^3\text{He}$ -pressure and active volume were taken or calculated from [21] . . . . .	28
3.5	Operating parameters of the Reuter Stokes $\text{BF}_3$ detector. . . . .	30
4.1	Peak areas and errors determined using the on-site software. 1 und 2 refer to the different Indium probes. . . . .	35
4.2	Peak areas and errors determined using InterSpec. 1 und 2 refer to the different Indium probes. . . . .	35
4.3	Peak areas and errors determined manually. 1 und 2 refer to the different Indium probes. . . . .	36
4.4	Collected neutron speeds and wavelengths. . . . .	42
4.5	Composition of the neutron beam, measured with two different neutron detectors without accounting for the different detection efficiencies at each wavelength. . . . .	46
4.6	Efficiency corrected composition of the neutron beam, measured with two different neutron detectors. . . . .	46
4.7	Manually calculated efficiency corrected composition of the neutron beam, measured with two different neutron detectors. . . . .	46
4.8	Relative detector efficiencies at the different occurring neutron speeds. 2200 m/s was kept as a reference. . . . .	48
4.9	Detector efficiencies estimated for thermal neutrons and calculated for the average beam composition as of Table 4.7. . . . .	48
4.10	Empirical efficiencies of all used detectors. The added numbers in the detector names for VacuTec Type 70 063 and Canberra 20NH20/1TP signify the internal numbering of the detectors at Atominstitut. . . . .	49
5.1	Predicted efficiencies of the cylindrical $^3\text{He}$ detectors for common aperture sizes. Width $w$ for rectangular/quadratic and radius $r$ for circular apertures. . . . .	55

## References

- [1] L. Thulliez et al. *Calibration of nuclear recoils at the 100 eV scale using neutron capture*. J. Instrum. 16 (2021) P07032.
- [2] H. Abele et al. *Observation of a Nuclear Recoil Peak at the 100 eV Scale Induced by Neutron Capture*. Phys. Rev. Lett. 130 (2023) 211802.
- [3] G. Angloher et al. *Exploring CE $\nu$ NS with NUCLEUS at the Chooz nuclear power plant*. Eur. Phys. J. C (2019) 79:1018.
- [4] J. Rothe et al. *NUCLEUS: Exploring Coherent Neutrino-Nucleus Scattering with Cryogenic Detectors*. Journal of Low Temperature Physics (2020) 199:433–440.
- [5] K. Irwin and G. Hilton. “Transition-Edge Sensors”. In: *Cryogenic Particle Detection*. Ed. by C. Enss. Berlin, Heidelberg: Springer Berlin Heidelberg, 2005, pp. 63–71. DOI: 10.1007/10933596\_3.
- [6] H. Kern. “Vermessung des Neutronenstrahls für das CRAB Projekt am Tangentialstrahlrohr des TRIGA Mark II Reaktors am Atominstitut”. Bachelor Thesis. TU Wien, 2023.
- [7] F. Engel. “Measuring and mapping of the neutron beam at the tangential beam tube at TRIGA Center Atominstitut, Vienna”. Project Thesis. TU Wien, 2023, pp. 8–9.
- [8] 2024. URL: [https://www-nds.iaea.org/relnsd/LCServlet?QRY=POPDECAY&DS\\_SEQNO=104276](https://www-nds.iaea.org/relnsd/LCServlet?QRY=POPDECAY&DS_SEQNO=104276).
- [9] Idaho National Engineering & Environmental Laboratory. *Gamma-Ray Spectrum Catalogue, Ge and Si Detector Spectra, Fourth Edition*. 1998.
- [10] M. Göbel. “Die Bestimmung des Selbstschirmfaktors einer Folie bei Einfall eines kollimierten Neutronenstrahls”. Project Thesis. TU Wien, 2021.
- [11] G. F. Knoll. *Radiation detection and measurement*. Hoboken, NJ : Wiley, 2010, pp. 55–57, 515, 518–520.
- [12] 2024. URL: <https://www-nds.iaea.org/relnsd/vcharthtml/VChartHTML.html>.
- [13] S. Mughabghab. *Atlas of neutron resonances: resonance parameters and thermal cross sections Z= 1-100*. 2006.
- [14] W. Chuirazzi, A. Craft, B. Schillinger, S. Cool, and A. Tengattini. “Boron-Based Neutron Scintillator Screens for Neutron Imaging”. In: *Journal of Imaging* 6 (2020). DOI: 10.3390/jimaging6110124.
- [15] C. Deng, Q. Hu, P. Li, Q. Wang, B. Xie, J. Yang, and X. Tuo. “Research on a Neutron Detector with a Boron-Lined Multilayer Converter”. In: *Applied Sciences* 14 (2024). DOI: 10.3390/app14104269.

- [16] S. Mehendale, K. Kanaki, M. Povoli, A. T. Samnøy, G. Tambave, A. Kok, C. Höglund, S. Schmidt, S. S. Kazi, I. Llamas-Jansa, T. Kittelmann, C.-C. Lai, T.-E. Hansen, S. Pospíšil, T. Slaviček, D. Röhrich, and R. Hall-Wilton. “Characterization of boron-coated silicon sensors for thermal neutron detection”. In: *Nuclear Instruments and Methods in Physics Research Section A: Accelerators, Spectrometers, Detectors and Associated Equipment* 972 (2020), p. 164124. DOI: <https://doi.org/10.1016/j.nima.2020.164124>.
- [17] M. M. Pickrell, A. Lavietes, V. Gavron, D. Henzlova, M. J. Joyce, R. Kouzes, and H. Menlove. “The IAEA Workshop on Requirements and Potential Technologies for Replacement of  $^3\text{He}$  Detectors in IAEA Safeguards Applications”. In: *JNMM, Journal of the Institute of Nuclear Materials Management* 41(2) (2013), pp. 14–29.
- [18] A. Edoardo, O. D’Agostino, E. Fermi, B. Pontecorvo, F. Rasetti, and E. Segrè. “Artificial radioactivity produced by neutron bombardment—II”. In: *Proc. R. Soc. Lond* 149 (1935), pp. 522–558. DOI: <http://doi.org/10.1098/rspa.1935.0080>.
- [19] 2024. URL: <https://github.com/sandialabs/InterSpec>.
- [20] VacuTec Meßtechnik GmbH. *VacuTec He-3 Neutron Detector Type 70 063*.
- [21] Canberra. *He3-Catalog*. 2003.
- [22] 2024. URL: [https://www.engineeringtoolbox.com/non-ideal-gas-van-der-Waals-equation-constants-gas-law-d\\_1969.html](https://www.engineeringtoolbox.com/non-ideal-gas-van-der-Waals-equation-constants-gas-law-d_1969.html).